

## 1 Calponin-Homology Domain mediated bending of membrane associated actin 2 filaments

3  
4  
5 Saravanan Palani, Mohan K. Balasubramanian\*, and Darius V. Köster\*

6  
7 Centre for Mechanochemical Cell Biology and Warwick Medical School, Division of Biomedical Sciences, CV4  
8 7AL Coventry, UK

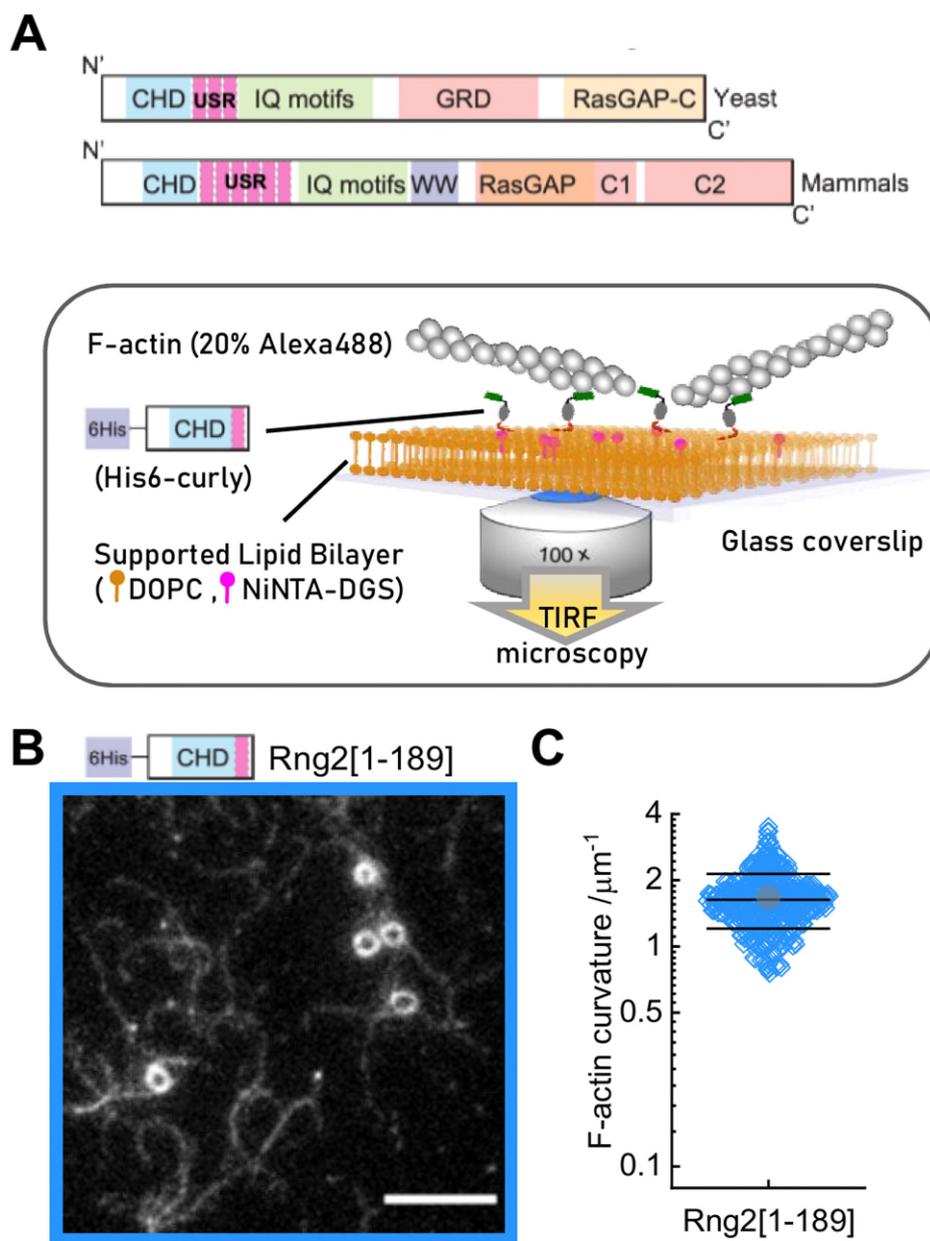
9 \* Corresponding authors: [M.K.Balasubramanian@warwick.ac.uk](mailto:M.K.Balasubramanian@warwick.ac.uk), [D.Koester@warwick.ac.uk](mailto:D.Koester@warwick.ac.uk)

10  
11  
12 **Actin filaments are central to numerous biological processes in all domains of life. Driven by the interplay with molecular motors, actin binding and actin modulating proteins, the actin cytoskeleton exhibits a variety of geometries. This includes structures with a curved geometry such as axon-stabilizing actin rings, actin cages around mitochondria and the cytokinetic actomyosin ring, which are generally assumed to be formed by short linear filaments held together by actin cross-linkers. However, whether individual actin filaments in these structures could be curved and how they may assume a curved geometry remains unknown. Here, we show that “curly”, a region from the IQGAP family of proteins from three different organisms, comprising the actin-binding calponin-homology domain and a C-terminal unstructured domain, stabilizes individual actin filaments in a curved geometry when anchored to lipid membranes. Whereas F-actin is semi-flexible with a persistence length of  $\sim 10 \mu\text{m}$ , binding of mobile curly within lipid membranes generates actin filament arcs and full rings of high curvature with radii below  $1 \mu\text{m}$ . Higher rates of fully formed actin rings are observed in the presence of the actin-binding coiled-coil protein tropomyosin, and also when actin is directly polymerized on lipid membranes decorated with curly. Strikingly, curly induced actin filament rings contract upon the addition of muscle myosin II filaments and expression of curly in mammalian cells leads to highly curved actin structures in the cytoskeleton. Taken together, our work identifies a new mechanism to generate highly curved actin filaments, which opens a new range of possibilities to control actin filament geometries, that can be used, for example, in designing synthetic cytoskeletal structures.**

13  
14  
15  
16  
17  
18  
19  
20  
21  
22  
23  
24  
25  
26  
27  
28  
29  
30  
31  
32  
33  
34  
35  
36 The IQGAP family of proteins plays a key role in actin cytoskeleton regulation including the assembly and function of the contractile actomyosin ring in budding and fission yeasts (Briggs & Sacks, 2003; Eng et al., 1998; Epp & Chant, 1997; Tebbs et al., 2013). To study the mechanism and role of actin binding by the fission yeast IQGAP (encoded by the *rng2* gene), we utilized a strategy to investigate its function when immobilized on supported lipid bilayers. We chose this approach, since during cytokinesis Rng2, which binds a number of actomyosin ring proteins, is tethered to the plasma membrane via Mid1 ensuring the formation and anchoring of the cytokinetic ring (Laplanche et al., 2016; Laporte et al., 2011; Padmanabhan et al., 2011). We linked hexa-histidine tagged *rng2* protein fragments to supported lipid bilayers containing nickel-chelating lipids (DOGS-NTA( $\text{Ni}^{2+}$ )) and observed the binding of fluorescently labelled actin filaments using live total internal reflection fluorescence (TIRF) microscopy as described earlier (Köster et al., 2016) (Figure 1A). The actin-binding calponin homology domain (CHD) is located at the N-terminus of Rng2 (AA 41-147), and the construct His<sub>6</sub>-Rng2[1-189] (subsequently referred to as curly) containing the CHD and additional 42 amino acids was found to bind actin filaments (Figure 1B, Figure 1-figure supplement 1A-C). Remarkably, when bound to His<sub>6</sub>-Curly a large fraction of actin filaments formed tightly bent rings ( $21 \pm 5$  rings per field of view) with a characteristic curvature  $C_{\text{curly}} = 1.7 \pm 0.5 \mu\text{m}^{-1}$  ( $N = 425$ ) (Figure 1 C; Figure 1 – figure supplement 1 D; Video 1). To our knowledge, this is an unprecedented phenomenon specific to curly. Binding of other membrane attached actin binding proteins in the same geometry does not appreciably bend actin ( $C_{\alpha\text{-actinin}} = 0.3 \pm 0.1 \mu\text{m}^{-1}$ ,  $N = 85$ ;  $C_{\text{EzrinABD}} = 0.5 \pm 0.3 \mu\text{m}^{-1}$ ,  $N = 127$ ) (Figure 1-figure supplement 2 A-D). Membrane anchored fimbrin has also been shown not to bend actin (Murrell & Gardel, 2012).

60

## Figure 1



61

62 **Figure 1 – Formation of actin filament rings by membrane tethered curly (Rng2[1-189])**

63 (A) Schematic representation of (top) the IQGAP proteins Rng2 (yeast, *S. pombe*) and  
64 IQGAP1 (mammals, *H. Sapiens*) and (bottom) the experimental setup used in this study;  
65 CHD - Calponin Homology Domain, USR – Unstructured Region, GRD - GAP Related  
66 Domain, RasGAP – Ras GTPase Activating Protein, WW – tryptophan containing protein  
67 domain.

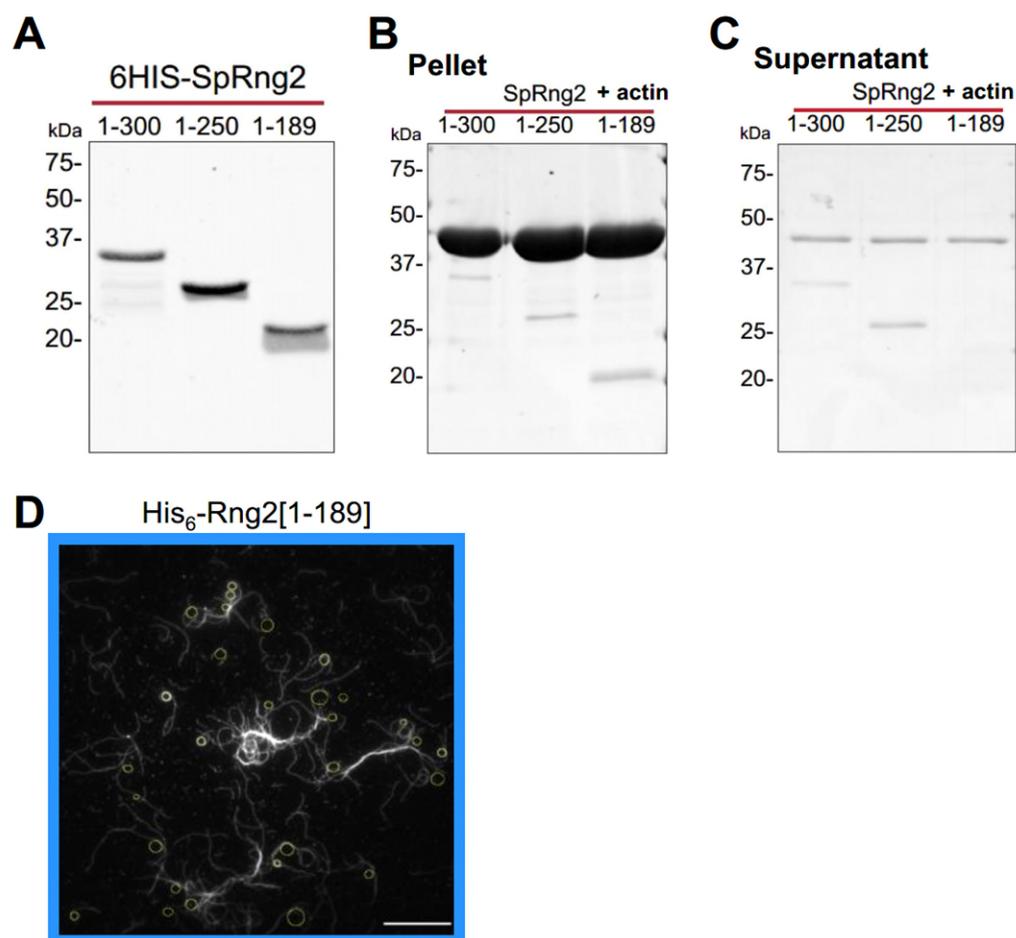
68 (B) TIRF microscopy image of actin filaments (Alexa488) bound to SLB tethered His<sub>6</sub>-curly;  
69 scale bar 5  $\mu\text{m}$ .

70 (C) Curvature measurements of actin filament rings and curved segments; shown are the  
71 individual data points and their mean  $\pm$  s.d.; N = 425 obtained from 8 field of views from  
72 4 individual experiments.

73

74

## Figure 1 - figure supplement 1

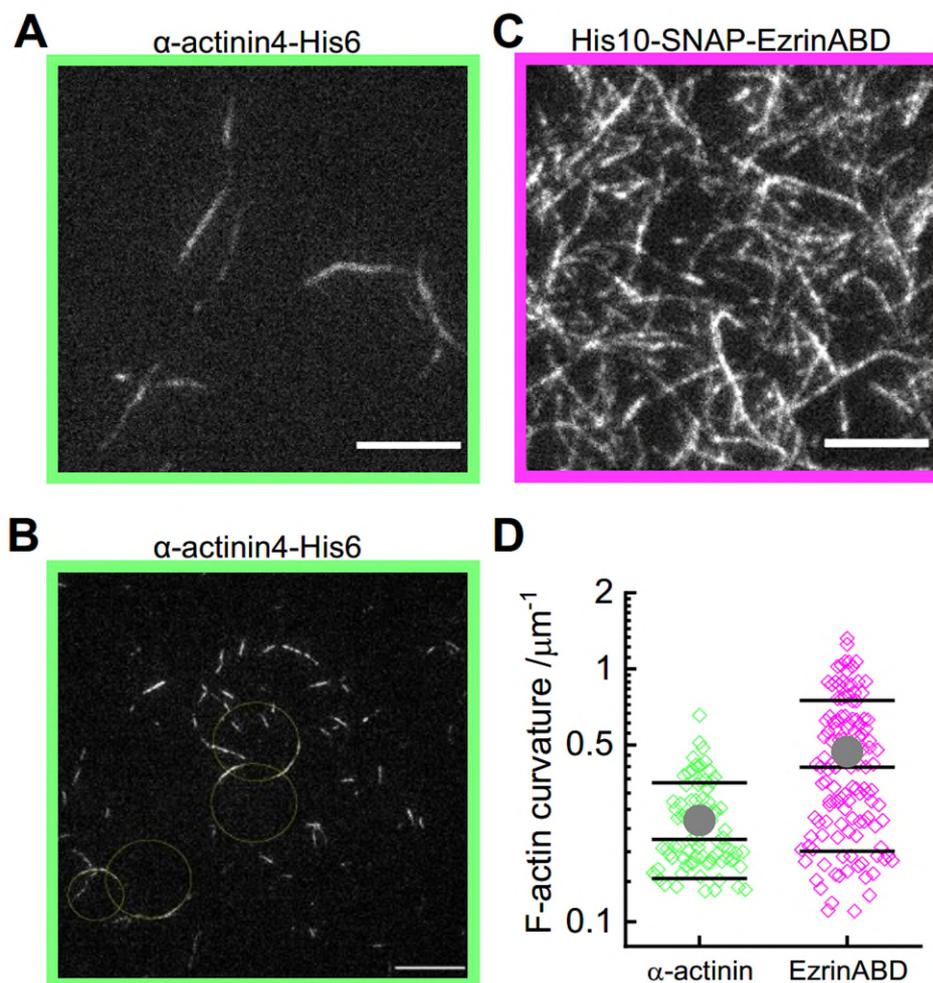


75  
76  
77  
78  
79  
80  
81  
82  
83  
84  
85  
86  
87  
88  
89  
90  
91  
92  
93  
94  
95  
96  
97  
98  
99

### Figure 1 - figure supplement 1

- (A) Western blot of the different His<sub>6</sub>-Rng2 constructs after protein purification.  
(B) SDS-PAGE of the actin filament pellet after incubation with His<sub>6</sub>-Rng2 constructs and centrifugation at 100,000g for 20 min at 25°C.  
(C) SDS-PAGE of the supernatant from the sample described in (B).  
(D) TIRF microscopy image of actin filaments (Alexa488) bound to SLB tethered His<sub>6</sub>- curly; circles show curvature measurements; scale bar 10 μm.

## Figure 1 - figure supplement 2



100  
101  
102  
103  
104  
105  
106  
107  
108  
109  
110  
111  
112  
113  
114  
115  
116  
117  
118  
119

### Figure 1-figure supplement 2

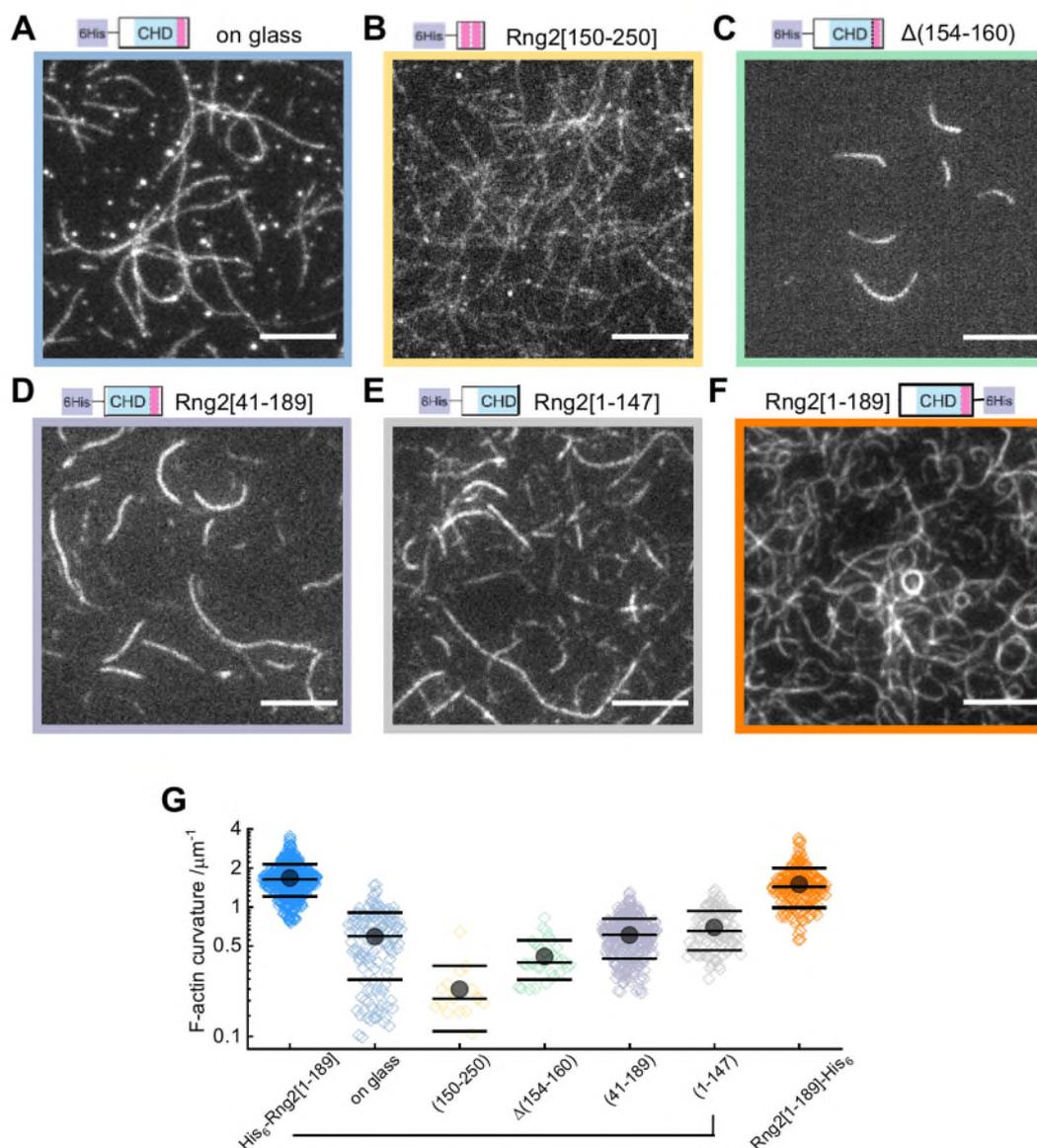
- (A) TIRF microscopy image of actin filaments (Alexa488) bound to SLB tethered  $\alpha$ -actinin-His<sub>6</sub>; scale bar 5  $\mu\text{m}$ .
- (B) TIRF microscopy image of actin filaments (Alexa488) bound to SLB tethered  $\alpha$ -actinin-His<sub>6</sub>; circles show curvature measurements; scale bar 10  $\mu\text{m}$ .
- (C) TIRF microscopy image of actin filaments (Alexa488) bound to SLB tethered His<sub>10</sub>-EzrinABD; scale bar 5  $\mu\text{m}$ .
- (D) Curvature measurements of actin filament rings and curved segments; shown are the individual data points and their mean  $\pm$  s.d.;  $\alpha$ -actinin-His<sub>6</sub>: N = 85 obtained from 10 field of views from 4 individual experiments; His<sub>10</sub>-EzrinABD : N = 127 obtained from 9 field of views from 3 individual experiments.

120 To understand the mechanism leading to actin filament bending and ring formation by curly,  
121 we tested the role of different fragments of curly and their orientation as well as curly  
122 anchoring to lipid membranes in actin filament bending. Curly mobility within planar lipid  
123 membranes was important for actin bending as glass adsorbed, immobilized His<sub>6</sub>-Curly  
124 displayed reduced actin bending and ring formation ( $C_{\text{glass}} = 0.6 \pm 0.3 \mu\text{m}^{-1}$ ,  $N = 138$ ) (Figure  
125 2 A, F), and when using membrane tethered fluorescently labelled His<sub>6</sub>-SNAP-curly, a weak  
126 accumulation of curly under actin filaments could be observed (Figure 2- figure supplement  
127 1). Next, we generated fragments of curly to discern the regions important for actin binding  
128 and bending. We found that the C-terminal region following the CHD (His6-Rng2[150-250])  
129 alone was able to bind actin filaments without inducing bending ( $C_{[150-250]} = 0.2 \pm 0.1 \mu\text{m}^{-1}$ ,  $N$   
130  $= 17$ ) (Figure 2 B). Interestingly, a 7AA deletion (Rng2[1-189]- $\Delta$ (154-160)) led to a reduced  
131 degree of actin binding and bending ( $C_{\Delta(154-160)} = 0.4 \pm 0.1 \mu\text{m}^{-1}$ ,  $N = 33$ ) (Figure 2 C).  
132 Similarly, the fragments Rng2[41-189] and Rng2[1-147] displayed weaker actin binding and  
133 bending compared to curly ( $C_{[41-189]} = 0.6 \pm 0.2 \mu\text{m}^{-1}$ ,  $N = 323$ ;  $C_{[1-147]} = 0.7 \pm 0.2 \mu\text{m}^{-1}$ ,  $N =$   
134  $118$ ) (Figure 2 D, E). The location of the hexa-histidine tag to link curly to the lipid membrane  
135 (C-terminal hexa-histidine tagged construct Rng2[1-189]-His<sub>6</sub>) did not affect actin filament  
136 bending ( $25 \pm 7$  rings per field of view;  $C_{\text{curly-his}} = 1.5 \pm 0.5 \mu\text{m}^{-1}$ ,  $N = 184$ ) (Figure 2 F). Taken  
137 together (Figure 2 G), this suggests that curly contains two actin binding sites, one located  
138 within the CHD followed by a second within Rng2[148-189]. Both actin binding sites are  
139 necessary for actin bending as neither Rng2[1-147] nor Rng2[150-250] caused strong  
140 bending. It is very likely that the second actin binding site includes the 7AA Rng2[154-160]  
141 as this unstructured region maps directly to AA 240-246 of the dystrophin CH2 domain  
142 (Wang et al., 2004). The first 40 AA of Rng2 are likely to be important for the protein folding  
143 and stability, because of which the Rng2[41-189] construct showed poor actin binding and  
144 did not lead to actin bending.

145  
146  
147  
148  
149  
150  
151  
152  
153  
154  
155  
156  
157  
158  
159  
160  
161  
162  
163  
164

165

**Figure 2**



166  
167

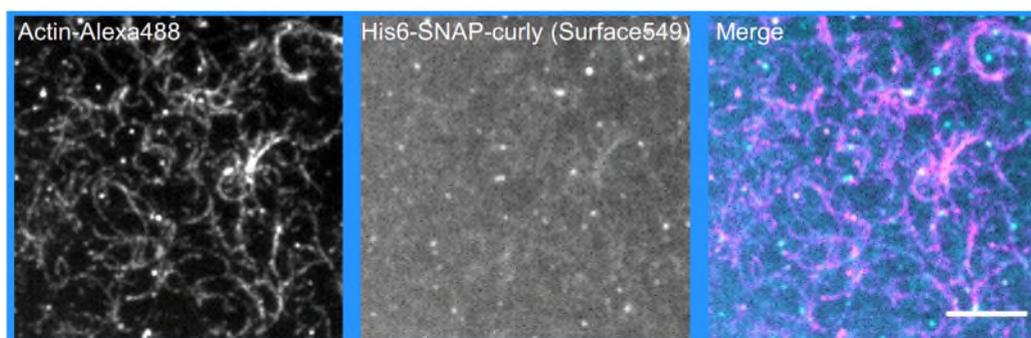
**Figure 2 - Characterization of actin binding and bending by fragments of curly**

TIRF microscopy images of actin filaments (Alexa488) bound to

- (A) glass adsorbed His<sub>6</sub>-curly; N = 138 from 9 field of views from 3 independent experiments;
  - (B) SLB bound His<sub>6</sub>-Rng2[150-250]; N = 144 from 10 field of views from 2 independent experiments;
  - (C) SLB bound His<sub>6</sub>-Rng2[1-189]Δ(154-160); N = 33 from 10 field of views from 2 independent experiments;
  - (D) SLB bound His<sub>6</sub>-Rng2[41-189]; N = 323 from 9 field of views from 3 independent experiments;
  - (E) SLB bound His<sub>6</sub>-Rng2[1-147]; N = 118 from 12 field of views from 2 experiments;
  - (F) SLB bound Rng2[1-189]-His<sub>6</sub>; N = 658 from 16 field of views from 4 experiments;
- Scale bars: 5 μm.
- (G) Curvature measurements of actin filament rings and curved segments; shown are the individual data points and their mean ± s.d.

183

## Figure 2 - figure supplement 1



184  
185  
186  
187  
188  
189  
190  
191  
192  
193  
194  
195  
196  
197  
198  
199  
200  
201  
202  
203  
204  
205  
206  
207  
208  
209  
210  
211  
212  
213  
214  
215  
216  
217  
218  
219  
220  
221  
222  
223  
224  
225

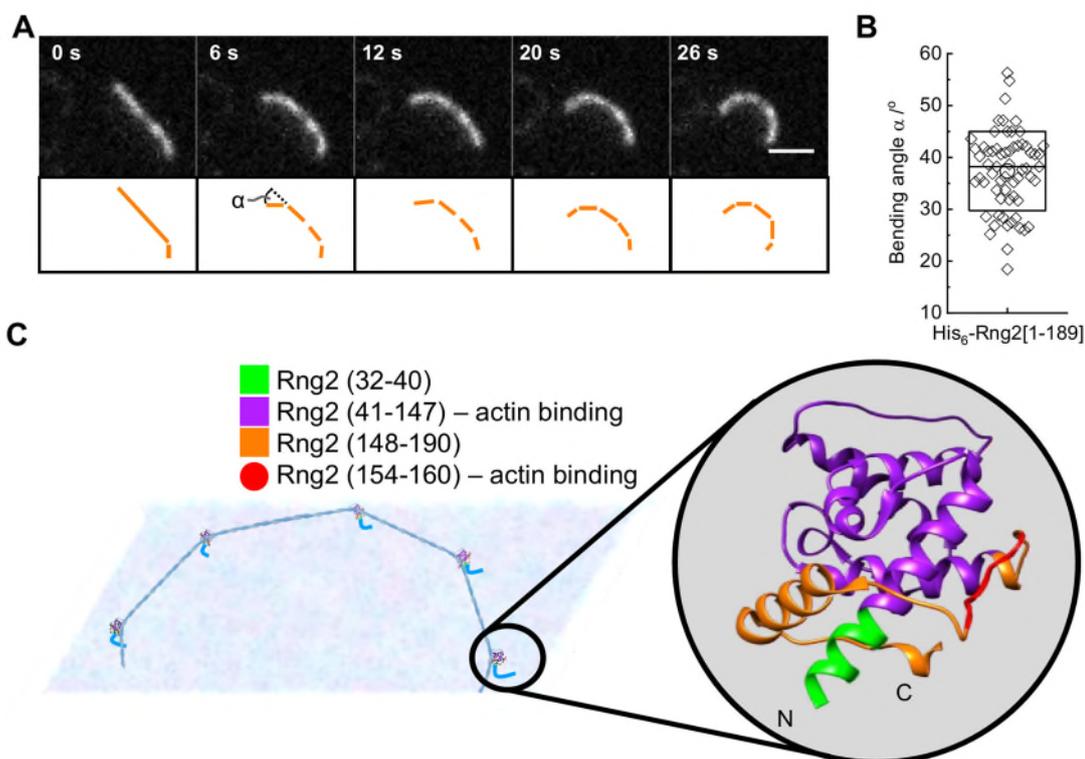
### Figure 2- supplement figure 1

Dual color TIRF microscopy image of actin filaments (Alexa488, magenta) bound to SLB tethered fluorescently labelled His<sub>6</sub>-SNAP-curly (Surface549, cyan); scale bar 5  $\mu$ m.

226 Careful examination of individual actin filaments bound to membrane tethered His<sub>6</sub>-Curly  
227 allowed us to identify the occurrence of discrete kinks of an angle  $\alpha = 37^\circ \pm 8^\circ$  (N = 63) along  
228 actin filaments during the transition from straight to bent filaments (Figure 2-figure  
229 supplement 2 A, B; Video 2). Based on the experimental data and the predicted molecular  
230 structure of curly (Rng2[1-189]) we hypothesize that i) the CHD (Rng2[41-147]) contains at  
231 least one actin binding site (similar to the utrophin actin binding domains ABD2' (UTRN[84-  
232 94]) and ABD2 (UTRN[107-126]) (Kumari et al., 2020)) and ii) the C-terminal extension from  
233 the CHD contains an additional actin binding site (including Rng2[154-160]) (Wang et al.,  
234 2004). The latter could lead to a change in the actin subunit orientation within the actin  
235 filament similar to the action of cofilin (Narita, 2020) and could lead to overall actin bending  
236 when the binding is asymmetric (Figure 2-figure supplement 2 C). However, in contrast to  
237 cofilin, we could not observe any events actin filament severing by curly.

238  
239  
240  
241  
242  
243  
244  
245  
246  
247  
248  
249  
250  
251  
252  
253  
254  
255  
256  
257  
258  
259  
260  
261  
262  
263  
264  
265  
266  
267  
268  
269  
270  
271  
272  
273  
274  
275  
276  
277  
278  
279  
280  
281  
282  
283

## Figure 2 - figure supplement 2



284  
285  
286  
287  
288  
289  
290  
291  
292  
293  
294  
295  
296  
297  
298  
299  
300  
301  
302  
303  
304  
305  
306  
307  
308  
309  
310  
311  
312  
313  
314  
315  
316

### Figure 2- supplement figure 2

- (A) TIRF microscopy image time series of an actin filament (Alexa488) bound to SLB tethered His<sub>6</sub>-curly and displaying stepwise bending; scale bar: 1  $\mu$ m.
- (B) Bending angles of individual bending events in actin filaments; shown are the individual data points and their mean  $\pm$  s.d.; N = 63 from 6 individual actin filaments.
- (C) Model representation of curly and how it could interact with actin to induce local bends in the actin filament; the inset shows curly with the regions tested in this study highlighted in color.

317 Next, we studied whether actin bending by curly depended on the orientation of actin  
318 filaments by following the landing of actin filaments decorated with labelled capping protein  
319 as a plus end marker (Bieling et al., 2016). We found that the bending was oriented anti-  
320 clockwise with respect to the plus end in all instances where the plus end was clearly  
321 labelled and the orientation of filament bending could be identified (Figure 3A, B; Figure 3-  
322 figure supplement 1 A, B). This was observed using both, the N-terminal and C-terminal  
323 hexa-histidine tagged curly indicating that the internal sequence of the two actin binding  
324 sites within curly sets the chirality of actin bending and not the position of the membrane  
325 linker (Figure 3A, B; Figure 3-figure supplement 1 A, B; Video 3, 4). Actin filaments  
326 appeared to bend concomitant with their landing on the supported lipid bilayer, which  
327 indicates that the bending did not require the full actin filament to be tethered to the SLB and  
328 underlined the earlier observation that the bending occurred locally.

329  
330 To decouple the actin filament bending from the landing of actin filaments, we induced  
331 polymerization of actin filaments at planar lipid membranes in the presence of membrane  
332 tethered curly (His<sub>6</sub>-Curly) by using membrane tethered formin (His<sub>6</sub>-SpCdc12(FH1-FH2)),  
333 profilin-actin and ATP. Strikingly, polymerizing actin filaments displayed characteristic  
334 bending shortly after the onset of polymerization and grew often into full rings ( $44 \pm 6$  rings  
335 per field of view,  $C_{\text{formin rings}} = 1.7 \pm 0.4 \mu\text{m}^{-1}$ ,  $N = 477$ ;  $C_{\text{formin short}} = 1.1 \pm 0.3 \mu\text{m}^{-1}$ ,  $N = 125$ )  
336 (Figure 3 C, D; Figure 3-figure supplement 1 C, D; Video 5). By contrast, polymerization of  
337 actin filaments along SLBs decorated with His<sub>10</sub>-SNAP-EzrinABD did not result in the  
338 formation of arcs and rings, establishing that actin filament bending was due to curly and not  
339 due to formin (Figure 3-figure supplement 1 E, F). These observations showed that actin  
340 bending occurs continuously due to the binding of membrane tethered curly and did not  
341 require the cross-linking of adjacent ends of the same filament as was observed with the  
342 actin cross-linker anillin (Kučera et al., 2020). Importantly, the uni-directional bending  
343 supports the hypothesis that the binding site of curly with actin filaments defines an  
344 orientation, and the propagation of a curved trajectory once established indicates a  
345 cooperative process.

346  
347 Actin filaments forming the cytokinetic ring in *S. pombe* are wrapped by the coiled-coil  
348 protein tropomyosin (Cdc8), while the actin cross-linker fimbrin is present outside the  
349 cytokinetic ring region in Arp2/3 generated actin patches and prevents tropomyosin of  
350 binding to actin filaments in these patches (Skau & Kovar, 2010). To find out whether the  
351 actin bending effect of curly is conserved in tropomyosin wrapped actin filaments, we  
352 incubated actin filaments with tropomyosin before adding them to His<sub>6</sub>-Curly containing  
353 SLBs. Strikingly, addition of tropomyosin to actin filaments increased the frequency of actin  
354 ring formation without affecting actin filament curvature ( $38 \pm 3$  rings per field of view;  
355  $C_{\text{tropomyosin}} = 1.4 \pm 0.6 \mu\text{m}^{-1}$ ,  $N = 204$ ), while actin filaments incubated with the actin cross-  
356 linker fimbrin displayed reduced bending and ring formation ( $3 \pm 2$  rings per field of view;  
357  $C_{\text{fimbrin}} = 0.6 \pm 0.4 \mu\text{m}^{-1}$ ,  $N = 407$ ) (Figure 3-figure supplement 2 A-E; Video 6). Thus, the  
358 tropomyosin Cdc8 and curly cooperate to enhance actin filament bending and ring formation.

359  
360 Interestingly, we could observe that long actin filaments coated with tropomyosin would trace  
361 consecutive rings around the same center while landing on curly decorated lipid  
362 membranes. Subtraction of the image after completion of the first round of actin filament  
363 landing into a ring from the image after the second round revealed that the second ring  
364 occupied the interior space of the first ring. In line with that, comparison of the intensity  
365 profiles perpendicular to the actin filament of the first and second round of ring formation  
366 revealed a widening of the profile towards the interior of the ring (Figure 3-figure supplement  
367 3 A, B). A similar effect could be observed in examples of actin filaments polymerized by  
368 membrane tethered formin in the presence of membrane tethered curly (Figure 3-figure  
369 supplement 3 C, D). This would suggest that curly can arrange long actin filaments into an  
370 inward oriented spiral.

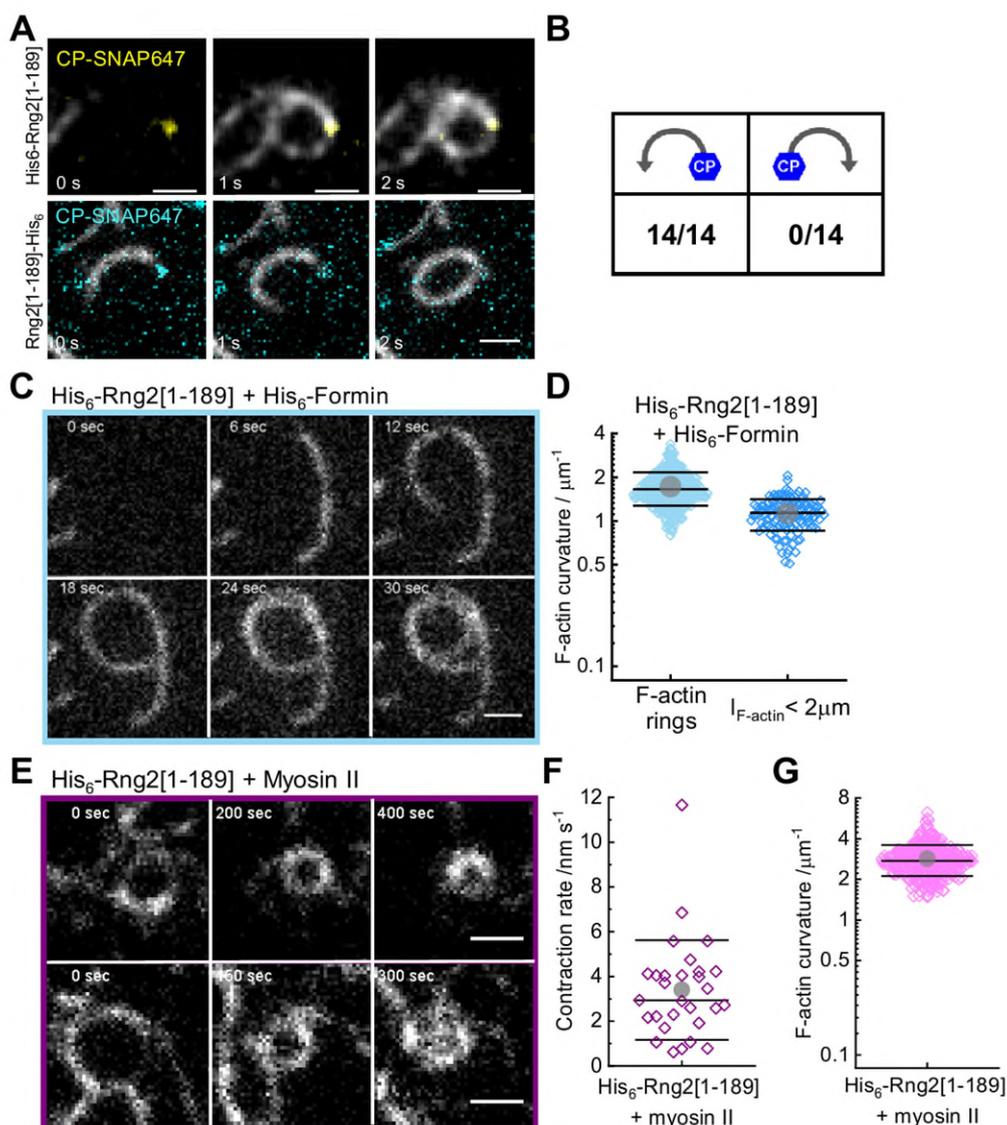
371  
372 To test whether the curly-induced actin rings can contract, we added rabbit skeletal muscle  
373 myosin II filaments and ATP to curly bound actin filaments and followed actin filament  
374 dynamics over time. After the myosin II filaments landed on the actin filaments, straight actin

375 filaments were propelled by myosin action and eventually started to bend and displayed a  
376 variety of dynamics including translation, rotation and finally contraction of actin rings (Figure  
377 3 E, Figure 3-figure supplement 4 A, Video 7). Interestingly, most actin rings displayed a  
378 counter-clockwise rotation (34/36 cases) and the contraction was slow with  $V_{\text{contraction}} = 3 \pm$   
379  $0.7 \text{ nm s}^{-1}$  ( $N = 29$ ) (Figure 3 F; Video 8). Despite reaching high curvatures of  $C_{\text{myoII}} = 2.8 \pm$   
380  $0.7 \mu\text{m}^{-1}$  ( $N = 342$ ) with a maximum of  $6.3 \mu\text{m}^{-1}$  there was no evidence of breaking of actin  
381 filaments during the contraction process (Figure 3 G). Additionally, the myosin II induced  
382 flows of actin filaments increased the formation of actin rings significantly ( $79 \pm 8$  rings per  
383 field of view) indicating that myosin II filament induced actin filament sliding enhanced the  
384 ability of membrane anchored curly to generate actin filament bending (Figure 3-figure  
385 supplement 4 B, C). In line with this, actin filament rings displayed increased localization of  
386 fluorescently labelled curly after addition of myosin II filaments action indicating that curly  
387 showed an increased affinity for highly bent actin and/ or stabilized actin filaments at higher  
388 curvatures (Figure 3-figure supplement 4 D). Interestingly, despite the observed high  
389 curvatures of actin filaments upon myosin II filament action, severing of actin filament was  
390 not observed suggesting that binding of curly reduces the rigidity of actin filaments.

391  
392 It was not obvious that addition of myosin II filaments would lead to actin ring constriction  
393 without the addition of any cross-linkers or other factors. When taking into account that curly  
394 arranges actin filaments into an inward spiral, a possible explanation for actin ring  
395 constriction would be that the myosin II filament acts both as a cross-linker and motor  
396 protein: one end of the myosin II filament sits at the actin filament plus end while other  
397 myosin head domains of the same myosin II filament pull along the same actin filament to  
398 travel towards the plus end leading to constriction (Figure 3-figure supplement 4 E). This  
399 would result in sub-optimal myosin head orientations towards the actin filament, which could  
400 explain the observed slow constriction rates that were orders of magnitude slower than the  
401 reported values for actin propulsion by myosin II in motility assays (Toyoshima et al., 1990).

402  
403  
404  
405  
406  
407  
408  
409  
410  
411  
412  
413  
414  
415  
416  
417  
418  
419  
420  
421  
422  
423  
424  
425  
426  
427  
428  
429

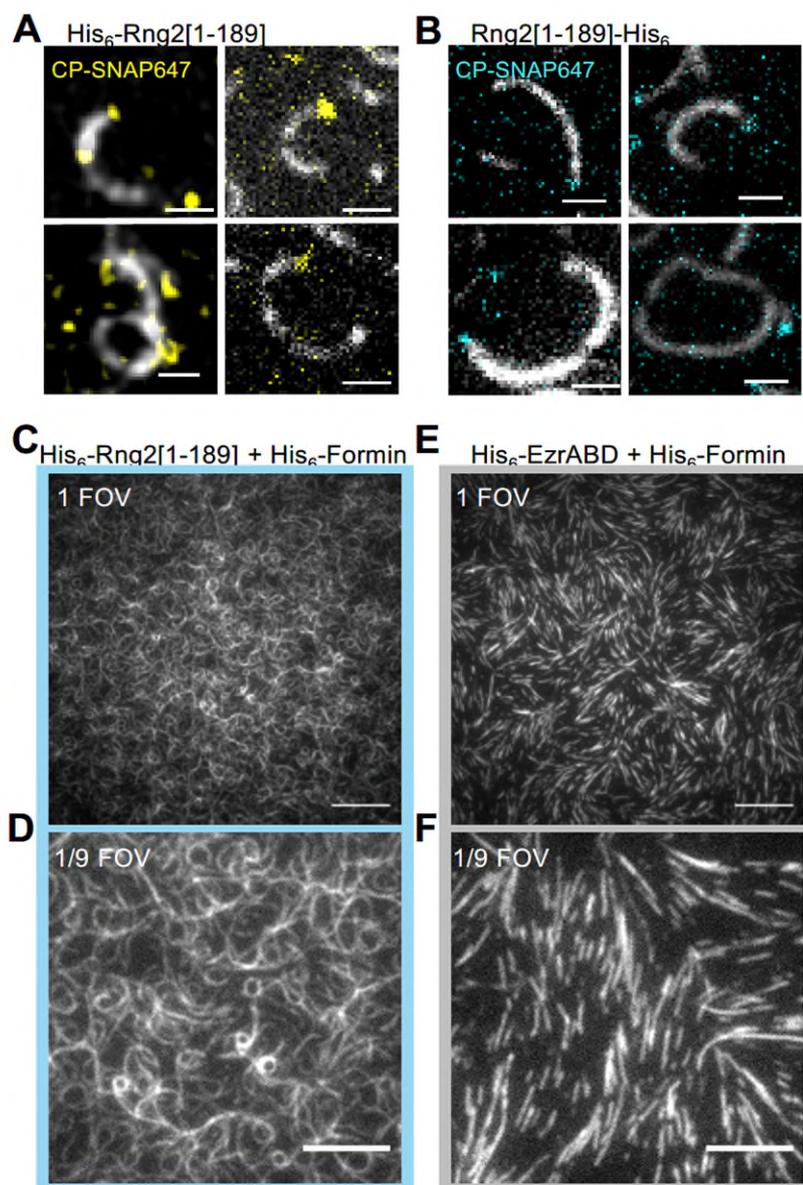
### Figure 3



430  
431 **Figure 3 – Curly recognizes actin filament orientation and enables actin ring contraction**  
432 **by myosin II**

433 (A) TIRF microscopy images of actin filaments (Alexa488) with the plus end marked with  
434 SNAP647-tagged capping protein binding to His<sub>6</sub>-curly (top) and curly-His<sub>6</sub> (bottom);  
435 scale bar: 1  $\mu\text{m}$ .  
436 (B) Count of actin filament bending orientations with respect to the capping protein where  
437 individual actin filaments could be identified.  
438 (C) TIRF microscopy images of a polymerizing actin filament (Alexa488) driven by  
439 membrane tethered His<sub>6</sub>-formin in the presence of His<sub>6</sub>-curly; scale bar: 1  $\mu\text{m}$ .  
440 (D) Curvature measurements of actin filament rings (light blue) and curved short actin  
441 filaments (< 2  $\mu\text{m}$ ; dark blue); shown are the individual data points and their mean  $\pm$   
442 s.d.;  $N_{\text{rings}} = 477$ ,  $N_{\text{short}} = 125$  from 9 field of views of 3 independent experiments.  
443 (E) TIRF microscopy images of actin filament (Alexa488) ring contraction after addition of  
444 muscle myosin II filaments on His<sub>6</sub>-curly containing SLBs; scale bar: 1  $\mu\text{m}$ .  
445 (F) Average contraction rates of actin filament rings after addition of muscle myosin II  
446 filaments; shown are the individual data points and their mean  $\pm$  s.d.;  $N = 18$  from 2  
447 individual experiments.  
448 (G) Curvature measurements of actin filament rings and curved segments 20 min after  
449 addition of myosin II filaments; shown are the individual data points and their mean  $\pm$   
450 s.d.;  $N = 342$  from 10 field of views of 2 individual experiments.

## Figure 3 - figure supplement 1

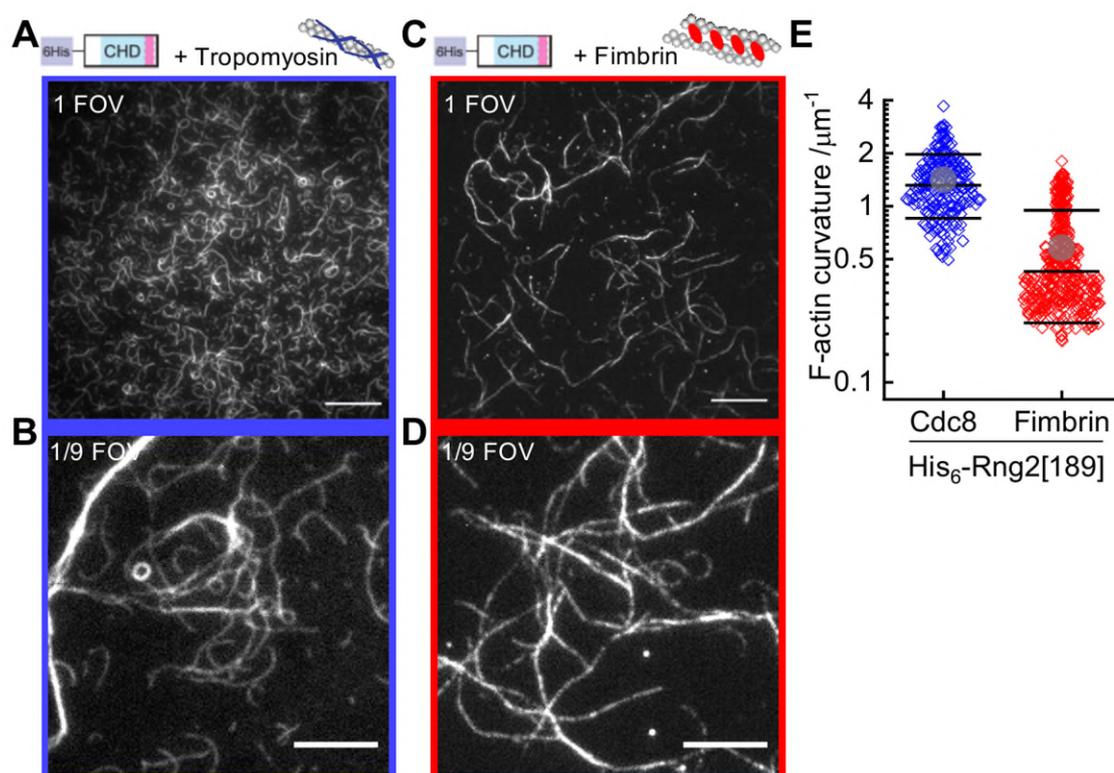


451  
452  
453  
454  
455  
456  
457  
458  
459  
460  
461  
462  
463  
464  
465  
466  
467  
468  
469  
470

### Figure 3-figure supplement 1

- (A) TIRF microscopy images of actin filaments (Alexa488) with the plus end marked with SNAP647-tagged capping protein binding to His<sub>6</sub>-curly; scale bar: 1 μm.
- (B) TIRF microscopy images of actin filaments (Alexa488) with the plus end marked with SNAP647-tagged capping protein binding to curly- His<sub>6</sub>; scale bar: 1 μm.
- (C) TIRF microscopy image (representing one field of view) of actin filaments (Alexa488) polymerized by membrane tethered His<sub>6</sub>-formin in the presence of His<sub>6</sub>-curly; scale bar: 10 μm.
- (D) TIRF microscopy image (representing 1/9 of the field of view) of actin filaments (Alexa488) polymerized by membrane tethered His<sub>6</sub>-formin in the presence of His<sub>6</sub>-curly; scale bar: 5 μm.
- (E) TIRF microscopy image (representing one field of view) of actin filaments (Alexa488) polymerized by membrane tethered His<sub>6</sub>-formin in the presence of His<sub>10</sub>-EzrinABD; scale bar: 10 μm.
- (F) TIRF microscopy image (representing 1/9 of the field of view) of actin filaments (Alexa488) polymerized by membrane tethered His<sub>6</sub>-formin in the presence of His<sub>10</sub>-EzrinABD; scale bar: 5 μm.

## Figure 3 - figure supplement 2

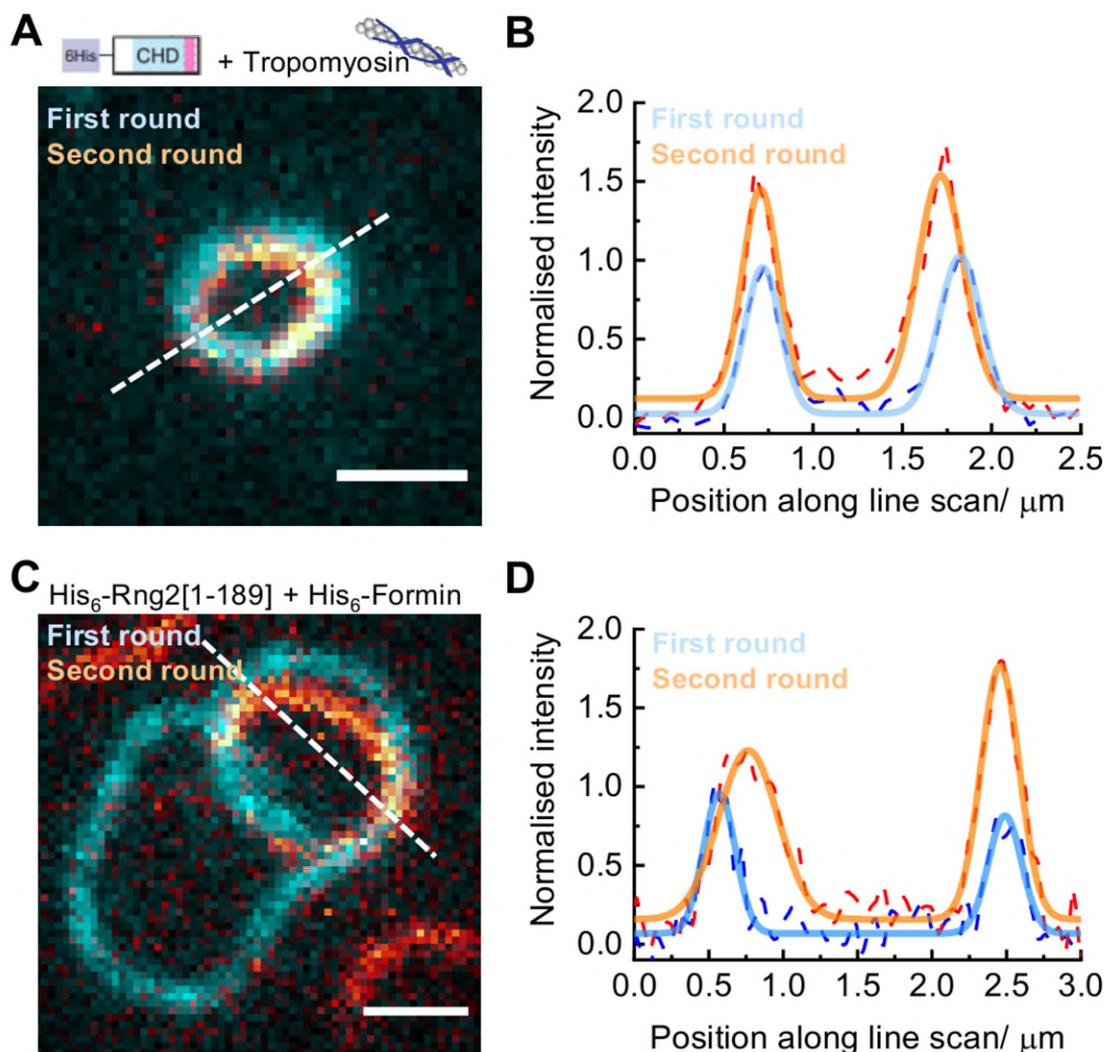


471  
472  
473  
474  
475  
476  
477  
478  
479  
480  
481  
482  
483  
484  
485  
486  
487  
488  
489  
490  
491  
492  
493  
494  
495  
496  
497  
498  
499  
500

### Figure 3-figure supplement 2

- (A) TIRF microscopy image (representing one field of view) of actin filaments (Alexa488) pre-incubated with tropomyosin (Cdc8) bound to membrane tethered His<sub>6</sub>-curly; scale bar: 10 μm.
- (B) TIRF microscopy image (representing 1/9 field of view) of actin filaments (Alexa488) pre-incubated with tropomyosin (Cdc8) bound to membrane tethered His<sub>6</sub>-curly; scale bar: 5 μm.
- (C) TIRF microscopy image (representing one field of view) of actin filaments (Alexa488) pre-incubated with fimbrin bound to membrane tethered His<sub>6</sub>-curly; scale bar: 10 μm.
- (D) TIRF microscopy image (representing 1/9 field of view) of actin filaments (Alexa488) pre-incubated with fimbrin bound to membrane tethered His<sub>6</sub>-curly; scale bar: 5 μm.
- (E) Curvature measurements of actin filament rings and curved segments; shown are the individual data points and their mean ± s.d.; tropomyosin (Cdc8, blue): N = 204 from 9 field of views of 3 individual experiments; fimbrin (red): N = 407 from 20 field of views of 3 individual experiments.

## Figure 3 - figure supplement 3



501  
502  
503  
504  
505  
506  
507  
508  
509  
510  
511  
512  
513  
514  
515  
516  
517  
518  
519  
520  
521  
522  
523

### Figure 3-figure supplement 3

- (A) TIRF microscopy image overlay showing multiple ring formation of a tropomyosin coated actin filament (Alexa488) during binding to membrane tethered His<sub>6</sub>-curly; the first ring formed is colored in cyan, the second ring (in orange) was highlighted by subtracting the image of the first ring from the image stack; scale bar: 1 μm.
- (B) Intensity line scan (3 pixels width) along the dashed line in (A) and corresponding Gaussian peak fits.
- (C) TIRF microscopy image overlay showing multiple ring formation of a polymerizing actin filament (Alexa488) by membrane tethered His<sub>6</sub>-formin in presence of membrane tethered His<sub>6</sub>-curly; the first ring formed is colored in cyan, the second ring (in orange) was highlighted by subtracting the image of the first ring from the image stack; scale bar: 1 μm.
- (D) Intensity line scan (3 pixels width) along the dashed line in (C) and corresponding Gaussian peak fits.

### Figure 3 - figure supplement 4

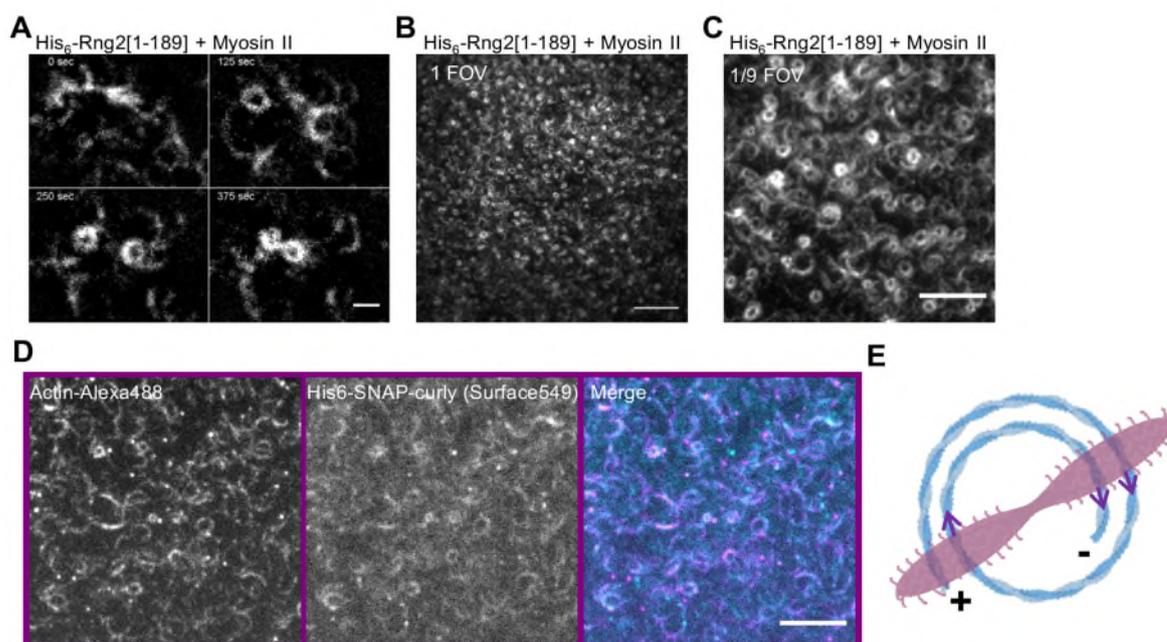


### Figure 3-figure supplement 4

- (A) TIRF microscopy image time series showing actin filament (Alexa488) ring formation, translation and contraction driven by myosin II filaments when bound to membrane tethered His<sub>6</sub>-curly; scale bar: 1 μm.
- (B) TIRF microscopy image (representing one field of view) of actin filaments (Alexa488) 20 min after addition of muscle myosin II filaments on His<sub>6</sub>-curly containing SLBs; scale bar: 10 μm.
- (C) TIRF microscopy image (representing one field of view) of actin filaments (Alexa488) 20 min after addition of muscle myosin II filaments on His<sub>6</sub>-curly containing SLBs; scale bar: 5 μm.
- (D) Dual color TIRF microscopy image of actin filaments (Alexa488, magenta) bound to membrane tethered fluorescently labelled His<sub>6</sub>-SNAP-curly (Surface549, cyan) 20 min after addition of myosin II filaments; scale bar 5 μm.
- (E) Model representing how myosin II filaments could drive the contraction of curly formed actin rings.

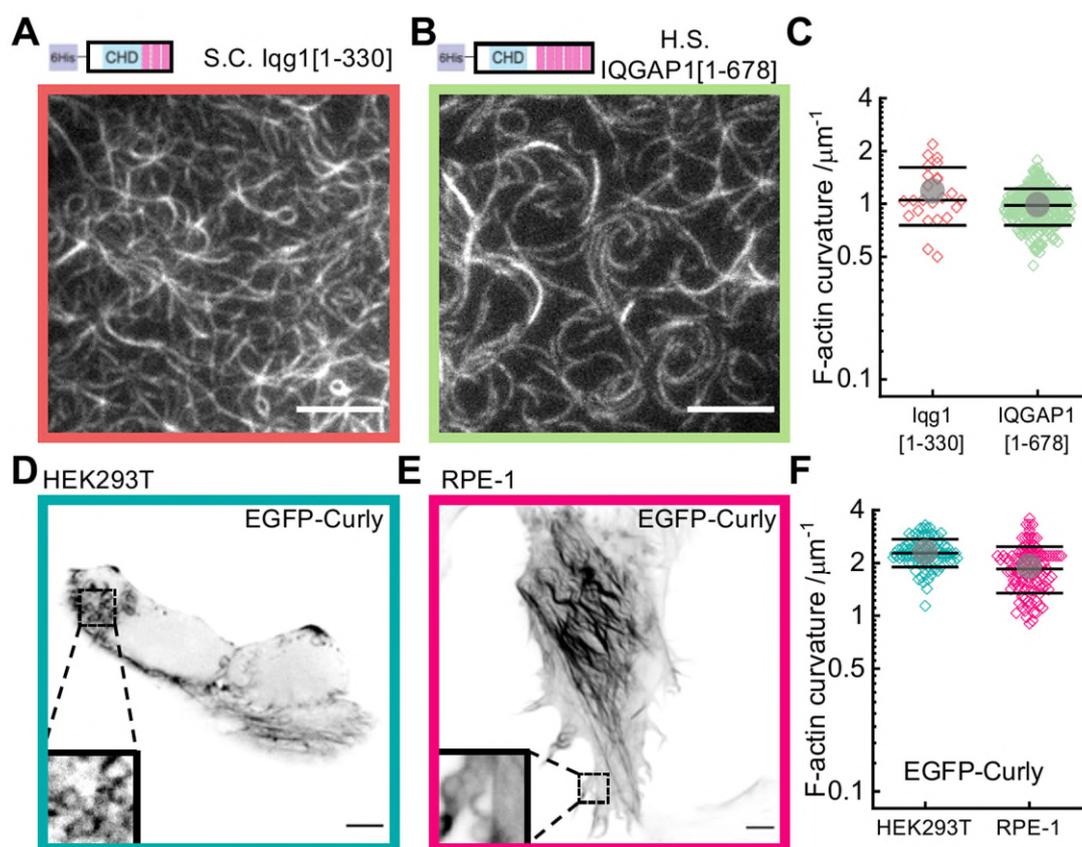
524  
525  
526  
527  
528  
529  
530  
531  
532  
533  
534  
535  
536  
537  
538  
539  
540  
541  
542  
543  
544  
545  
546  
547  
548  
549  
550  
551  
552  
553  
554  
555  
556  
557  
558  
559  
560

561 Since Rng2 belongs to the IQGAP protein family, we tested the N-terminal hexa-histidine  
562 tagged fragments of the IQGAP proteins Iqg1[1-330] (*S. cerevisiae*) and IQGAP1[1-678] (*H.*  
563 *sapiens*) and found that the bending of actin filaments was conserved ( $C_{S.C.} = 1.1 \pm 0.4 \mu\text{m}^{-1}$ ;  
564  $N = 110$ ;  $C_{H.S.} = 1.0 \pm 0.2 \mu\text{m}^{-1}$ ;  $N = 290$ ) (Figure 4 A-C). Comparison of the available crystal  
565 structures of *H. sapiens* IQGAP1[28-190] with *S. pombe* Rng2[32-190] indicates a high  
566 similarity between the two (Figure 4-figure supplement 1).

567  
568 Finally, to test the effect of curly on the actin cortex in cells, we expressed curly-EGFP in the  
569 mammalian cell lines HEK293T and RPE-1, which resulted in obvious changes in the actin  
570 cortex architecture with prominent occurrence of curved actin filaments and bundles with  
571 curvatures of  $C_{HEK293T} = 2.3 \pm 0.4 \mu\text{m}^{-1}$  ( $N = 91$  from 14 cells), and  $C_{RPE-1} = 1.9 \pm 0.6 \mu\text{m}^{-1}$  ( $N$   
572  $= 113$  from 11 cells) (Figure 4D-F). Co-expression with LifeAct-mCherry confirmed that  
573 EGFP-Curly bound to actin filaments in cells (Figure 4-figure supplement 2). These  
574 experiments established that curly could instructively reorganize actin filaments / networks  
575 into curved structures and rings.

576  
577  
578  
579  
580  
581  
582  
583  
584  
585  
586  
587  
588  
589  
590  
591  
592  
593  
594  
595  
596  
597  
598  
599  
600  
601  
602  
603  
604  
605  
606  
607  
608  
609  
610  
611  
612  
613  
614  
615  
616  
617  
618

## Figure 4

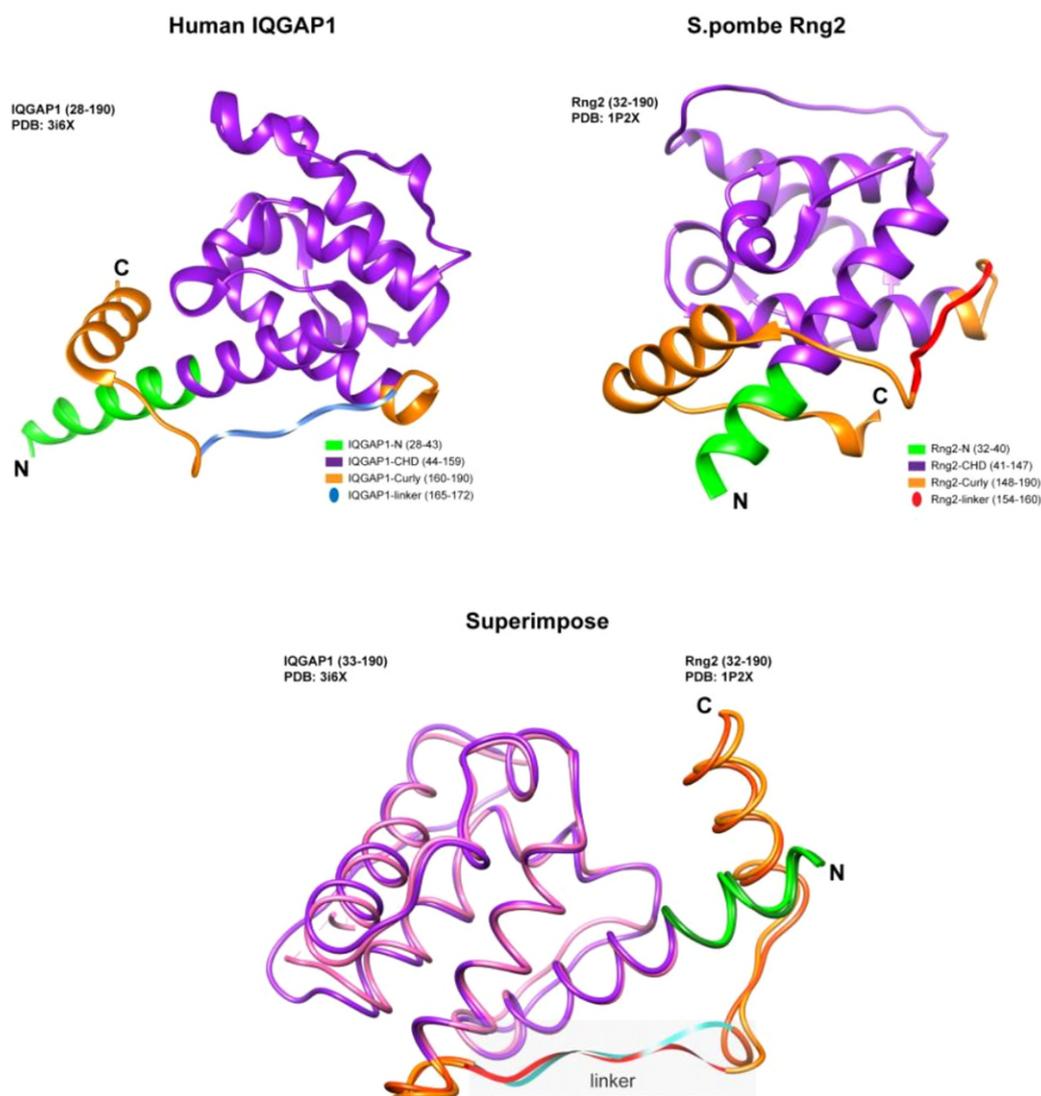


619  
620  
621  
622  
623  
624  
625  
626  
627  
628  
629  
630  
631  
632  
633  
634  
635  
636  
637  
638  
639  
640  
641  
642  
643  
644  
645  
646  
647  
648

### Figure 4 - Curly effect is conserved among species and it can foster actin bending in mammalian cells

- (A) TIRF microscopy image of actin filaments (Alexa488) bound to membrane tethered His6-Iqg1[1-330] (*S. cerevisiae*); scale bar: 5  $\mu\text{m}$ .
- (B) TIRF microscopy image of actin filaments (Alexa488) bound to membrane tethered His6-IQGAP1[1-678] (*H. sapiens*); scale bar: 5  $\mu\text{m}$ .
- (C) Curvature measurements of actin filament rings and curved segments; shown are the individual data points and their mean  $\pm$  s.d.; Iqg1[1-330] (orange): N = 167 from 12 field of views of 4 individual experiments; IQGAP1[1-678] (green): N = 407 from 20 field of views of 3 individual experiments.
- (D) Confocal microscopy image (average intensity projection of the basal cell section) of a HEK293T cell transfected with EGFP-Curly, inlet shows zoom of dashed box; scale bar: 5  $\mu\text{m}$ .
- (E) Confocal microscopy image (average intensity projection of the basal cell section) of a REP-1 cell transfected with EGFP-Curly, inlet shows zoom of dashed box; scale bar: 5  $\mu\text{m}$ .
- (F) Curvature measurements of actin filament rings and curved segments found in EGFP-Curly expressing cells; shown are the individual data points and their mean  $\pm$  s.d.; HEK293T (teal): N 91 from 14 cells of 2 individual experiments; REP-1 (fuchsia): N = 113 from 11 cells of 2 individual experiments.

## Figure 4 – figure supplement 1



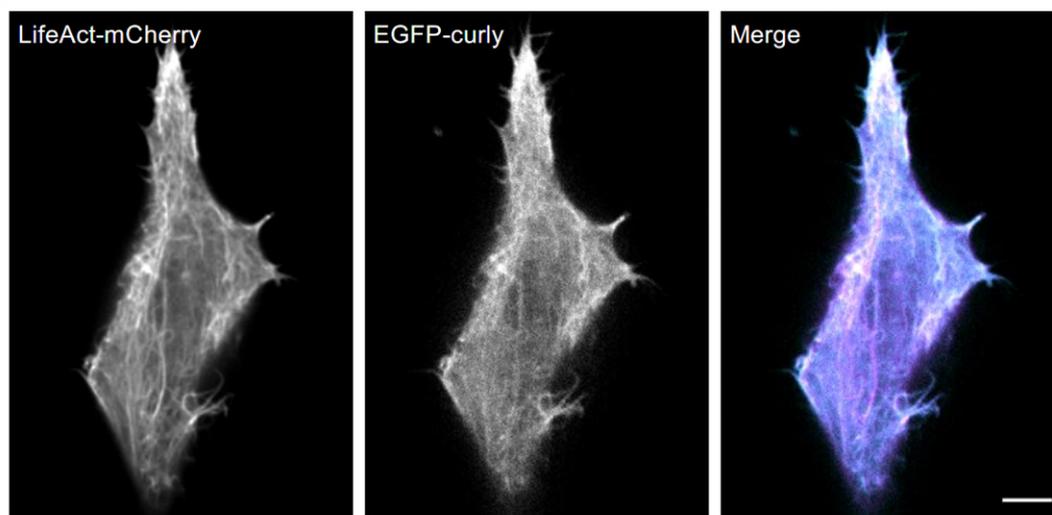
649  
650  
651  
652  
653  
654  
655  
656  
657  
658  
659  
660  
661  
662  
663  
664  
665  
666  
667  
668  
669  
670

### Figure 4-figure supplement 1

Depiction of structure predictions and overlay of *H. sapiens* IQGAP1[28-190] and *S. pombe* Rng2[32-190] indicating the strong similarity between the linker regions of both proteins that are thought to be important for actin bending.

## Figure 4 – figure supplement 2

A



671  
672  
673  
674  
675  
676  
677  
678  
679  
680  
681  
682  
683  
684  
685  
686  
687  
688  
689  
690  
691  
692  
693  
694  
695  
696  
697  
698  
699  
700  
701  
702  
703  
704  
705  
706  
707  
708

### Figure 4-figure supplement 2

Dual color confocal microscopy image (average intensity projection of the basal cell section) of a HEK293T cell transfected with LifeAct-mCherry (magenta) and EGFP-Curly (cyan); scale bar: 5  $\mu$ m.

## 709 Discussion

710  
711 Our results show that the N-terminal CHD of IQGAP proteins induces actin filament bending  
712 when tethered to lipid membranes, which constitutes a new type of actin binding protein and  
713 could be an important link between actin and membrane geometries. Recently, Uyeda and  
714 colleagues reported that curly (Rng2[1-189]) in solution can induce kinks at random  
715 locations of the actin filament (Hayakawa et al., 2020). This together with our results  
716 indicates that curly that is constrained to a lipid membrane, would bind asymmetrically to  
717 actin filaments leading to a succession of kinks towards the same direction leading to curling  
718 of the actin filaments into rings in the plane of the lipid membrane. With an estimated His<sub>6</sub>-  
719 Curly surface density on SLBs of 5000  $\mu\text{m}^{-2}$  (Köster et al., 2016; Nye & Groves, 2008) the  
720 approximated curly to actin ratio would be 1:7 or higher. The mobility of curly on the SLB  
721 allowing accumulation under actin filaments was important for continuous actin filament  
722 bending into rings as glass-immobilized curly failed to generate rings. In line with this, curly  
723 in solution, i.e. in the absence of a substrate providing confinement, did not lead to  
724 persistent bending of actin filaments (Hayakawa et al., 2020). Interestingly, individual  
725 transient kinks of an average angle of  $37^\circ \pm 8^\circ$  could be observed during actin filament  
726 binding to curly, but it remained unclear whether this is caused by binding of single or  
727 multiple proteins. Based on the data of the Utrophin-CHD actin binding sites (Kumari et al.,  
728 2020) together with the newly identified actin binding region within Rng2[150-189], the local  
729 change of the actin filament structure induced by curly could be similar to the effect of cofilin  
730 (Narita, 2020) allowing the formation of actin rings with curvatures that would be  
731 energetically unfavorable given the actin filament persistence length of 10  $\mu\text{m}$  (De La Cruz &  
732 Gardel, 2015). The increased flexibility of actin filaments is highlighted by the fact that  
733 addition of rabbit muscle myosin II filaments resulted in actin ring constriction without any  
734 evidence for filament rupture up to curvatures of  $6.3 \mu\text{m}^{-1}$  which is much higher than  
735 expected for actin alone (Taylor et al., 2000). This mechanism of actin ring formation stands  
736 out as it bends individual actin filaments in contrast to other reported systems that generate  
737 actin rings made of bundles of actin filaments (Litschel et al., 2020; Mavrakis et al., 2014;  
738 Mishra et al., 2013; Way et al., 1995).

739  
740 In case of *S. pombe* cytokinetic ring formation, Rng2 is localized at the plasma membrane  
741 by interaction with Mid1 via its C-terminal RAS-GAP and GRD domains (Almonacid et al.,  
742 2011; Padmanabhan et al., 2011) leaving the N-terminal CHD facing the cytoplasm and  
743 allowing interaction with actin filaments. Formin based polymerization of actin filaments is  
744 essential for cytokinetic ring formation and binding of the tropomyosin Cdc8 supports myosin  
745 driven cytokinetic ring contraction. Our work recapitulates that this minimal set of proteins  
746 can indeed generate and stabilize actin filaments of the right curvature to form the  
747 cytokinetic ring along the short axis of *S. pombe*. Even though electron microscopy data of  
748 the cytokinetic ring does not provide clear evidence of bent actin filaments (Swulius et al.,  
749 2018), this mechanism could work together with other processes such as cross-linkers  
750 ensuring the binding of fresh actin filaments along existing ones (Li & Munro, 2020) to drive  
751 robust formation of cytokinetic rings.

752  
753 Highly bent actin filament structures are most likely important for many cellular structures  
754 such as axons (Vassilopoulos et al., 2019; Xu et al., 2013) and mitochondrial actin cages  
755 (Kruppa et al., 2018), but the molecular mechanisms leading to their formation are still poorly  
756 understood. Future work could provide insights whether curly plays a role in actin ring  
757 formation in axons and around mitochondria. In addition, our system of membrane bound  
758 curly, actin filaments, and myosin II filaments constitutes a minimalistic system for actin ring  
759 formation and constriction and could be used in future to design synthetic dividing vesicles  
760 and further exiting active membrane-cortex systems.

761  
762  
763  
764  
765  
766

767 **Materials and Methods:**

768

769 **Cloning and Protein purification**

770

771 *S. pombe* Rng2 fragments, Fim1, Cdc12 (FH1-FH2) and *S. cerevisiae* Igg1 were amplified  
772 from cDNA library and genomic DNA respectively. Amplified fragments were cloned into pET  
773 (6His) and pGEX (GST) based vectors using Gibson cloning method (NEB builder, E5520S).  
774 Plasmids used in this study is listed in Table S1.

775

776 All protein expression plasmids were transformed into *E. coli* BL21-(DE3). Single colony was  
777 inoculated in 20 ml of LB media supplemented with appropriate antibiotic (pET-Kanamycin;  
778 pGEX-Ampicillin). Precultures were grown for ~12-16 h at 36 °C shaking at 200 r.p.m. Cells  
779 were diluted to OD<sub>600</sub> of 0.1 a.u. in 500 ml of LB with antibiotics and protein expression was  
780 induced with 0.25 mM isopropyl β-D-1-thiogalactopyranoside (IPTG). Protein was expressed  
781 for 3-4 h at 30 °C shaking at 200 r.p.m. unless otherwise noted. After induction cell pellets  
782 were collected and spun down at 7,000 r.p.m for 20 minutes after induction at 4 °C. Media  
783 was aspirated and pellets were washed once with cold phosphate buffered saline (PBS) with  
784 1mM phenylmethylsulfonyl fluoride (PMSF), and pellets were stored at -80 °C.

785

786 His tagged protein (His6-Rng2, Igg1 and Iggap1) purification: Cell pellets for purification  
787 were thawed on ice for 10 minutes. The pellets were resuspended in 10 ml of lysis buffer for  
788 sonication (50 mM Napi pH 7.6, 200 mM NaCl, 10mM Imidazole pH 7.5, 0.5 mM EDTA,  
789 1 mM DTT, 1 mg/ ml lysozyme, and complete mini-EDTA-Free protease inhibitor cocktail  
790 tablets) and incubated on ice for 20 min, followed by sonication (8 cycles, 15 sec pulse). The  
791 lysates were centrifuged at 14000 r.p.m, 30 min, 4 °C and the clarified lysate was transferred  
792 to a 15-ml tube. The 400 μl slurry of HisPur™ Ni-NTA agarose resin (cat. no. 88221, Thermo  
793 fisher) was washed with wash buffer (5x) (50 mM Napi (pH 7.6), 300 mM NaCl, 30mM  
794 Imidazole pH 7, 0.5 mM EDTA and 1 mM DTT) before the lysate was added. The clarified  
795 lysate was added to the washed Ni-NTA resin and incubated for 2h at 4 °C. After incubation  
796 with NiNTA resin, beads were washed with wash buffer 6-8 times in BIO-RAD prepaced  
797 column. Protein was eluted using Ni-NTA elution buffer (50 mM NaPi pH 7.6, 300 mM NaCl,  
798 0.5 mM EDTA, 1 mM DTT and 500 mM imidazole) and 300 μl elutions were collected in a  
799 clean Eppendorf tubes. Each fraction was assessed by SDS–polyacrylamide gel  
800 electrophoresis (SDS–PAGE). The eluates (E1-E3) were pooled, concentrated and buffer  
801 exchanged into the protein storage buffer (50 mM Tris-HCl pH 7.4, 150 mM NaCl, 1 mM DTT  
802 and 10% glycerol) using a PD MiniTrap G-25 sephadex columns (GE Healthcare) and the  
803 protein was stored at -80 °C. The protein concentration was estimated by UV280 and by  
804 comparing known quantities of BSA standards on an SDS–PAGE gel.

805

806 GST tagged protein (GST-Fim1) purification: Cell pellets for purification were thawed on ice  
807 for 10 minutes. The pellets were resuspended in 10 ml of lysis buffer for sonication (PBS,  
808 0.5 mM EDTA, 1 mM DTT, 1 mg/ ml lysozyme, and complete mini-EDTA-Free protease  
809 inhibitor cocktail tablets) and incubated on ice for 20 min, followed by sonication (10 cycles,  
810 15 sec pulse). After sonication cell lysate was incubated with 0.5% Triton-X-100 for 20  
811 minutes on ice. The lysates were centrifuged at 22000xg, 30 min, 4 °C and the clarified  
812 lysate was transferred to a 15-ml tube. The 400 μl slurry of glutathione sepharose-4B resin  
813 (cat. no. GE17-0756-01, GE) was washed with wash buffer (5x) (PBS, 0.5 mM EDTA and  
814 1 mM DTT) before the lysate was added. The clarified lysate was added to the washed  
815 glutathione sepharose resin and incubated for 2-3h at 4 °C. After incubation with sepharose  
816 resin, beads were washed with wash buffer 6-8 times in poly-prep chromatography columns  
817 (BIO-RAD laboratories Inc). Protein was eluted using GST elution buffer (50 mM Tris-HCl  
818 pH8.0 and 10 mM glutathione). Purified protein sample was quantified and stored in the  
819 storage buffer as described above in the previous section.

820

821 Acetylation mimicking version of tropomyosin (ASCdc8) was expressed in BL21-DE3 and  
822 protein was purified by boiling and precipitation method as described earlier (Palani et al.,  
823 2019; Skoumpla et al., 2007). Purified tropomyosin was dialyzed against the storage buffer

824 (50 mM NaCl, 10 mM imidazole, pH 7.5, and 1 mM DTT), flash frozen in liquid N<sub>2</sub> and  
825 stored at -80 °C.

826

827 SNAP labelling (SNAP-Surface® 549, S9112S, NEB) of capping protein-beta and Rng2 1-  
828 189 was performed as per the manufactures protocol.

829

### 830 **Co-sedimentation assay and Immunoblot**

831

832 Co-sedimentation assays were performed at 25°C by mixing 3 µM actin with different Rng2  
833 fragments, Scloq1(1-330) and Hs IGAP1 (1-678), and then spun at 100,000 g (high speed)  
834 for 20 min at 25°C. Equal volumes of supernatant and pellet were separated by 12% SDS-  
835 PAGE gel and stained with Coomassie blue (SimplyBlueStain, Invitrogen) or immunoblotted.  
836 For western analysis, equal volumes of each sample were diluted in 1 x Laemmli buffer (Bio-  
837 Rad). Samples were run on a hand cast 10-well 12% acrylamide gels (Bio-Rad), transferred  
838 onto nitro cellulose membranes and blotted with 1:1000 Anti-His-HRP (6xHis Epitope TAG,  
839 Cat. no. sc-8036 HRP, Santa Cruz Inc) and 1:500 anti-actin-HRP (cat. no. sc-47778 HRP,  
840 Santa Cruz Inc). Signal was detected by enhanced chemiluminescence (Clarity western  
841 ECL, Bio-Rad) imaged on a ChemiDoc MP (Bio-Rad).

842

### 843 **Mammalian expression**

844

845 *S. pombe* Rng2 fragment (1-189) was cloned into pCDNA3.1-eGFP using gibbon cloning  
846 method. HEK293 and RPE1 cells were transiently transfected with pCDNA3 containing  
847 SpRng2 (1-189) using Lipofectamine 2000 (cat. no. 11668019, Life Technologies) following  
848 manufacturer's instructions. Cells were transfected at ~70% confluency for 24 h before the  
849 experiments. For each imaging condition, 500,000 cells were transfected with 1 µg of DNA.  
850 Cells were seeded and imaged on µ-Dish 35 mm (cat. no. 81156, IBIDI). Before imaging, the  
851 culture medium was replaced with phenol red-free DMEM (Opti-MEM, cat. no. 31985062,  
852 Life Technologies). Images were taken using spinning disk microscope with a 100x Apo  
853 objective, NA 1.4.

854

### 855 **In vitro assay and Total Internal Reflection Fluorescence (TIRF) microscopy**

856

#### 857 *Supported Lipid Bilayer and Experimental Chamber Preparation*

858 The sample preparation, experimental conditions and lipid composition were similar to the  
859 ones described in previous work [Koester et al, 2016]. Glass coverslips (#1.5 borosilicate,  
860 Menzel, cat. no. 11348503, Fisher Scientific) for SLB formation were cleaned with  
861 Hellmanex III (Hellma Analytics, cat. No. Z805939, Merck) following the manufacturer's  
862 instructions followed by thorough rinses with EtOH and MilliQ water and blow dried with N<sub>2</sub>  
863 gas. For the experimental chamber, 0.2 ml PCR tubes (cat. no. I1402-8100, Starlab) were  
864 cut to remove the lid and conical bottom part. The remaining ring was stuck to the cleaned  
865 glass using UV glue (cat. no. NOA88, Norland Products) and three minutes curing by  
866 intense UV light at 265 nm (UV Stratalinker 2400, Stratagene). Freshly cleaned and  
867 assembled chambers were directly used for experiments.

868 Supported lipid bilayers (SLB) containing 98% DOPC (cat. no. 850375, Avanti Polar Lipids)  
869 and 2% DGS-NTA(Ni<sup>2+</sup>) (cat. no. 790404, Avanti Polar Lipids) lipids were formed by fusion  
870 of small uni-lamellar vesicles (SUV) that were prepared by lipid extrusion using a membrane  
871 with 100 nm pore size (cat. no. 610000, Avanti Polar Lipids). SLBs were formed by addition  
872 of 10 µl of SUV mix (at 4 mM lipid concentration) to chambers filled with 90 µl KMEH (50 mM  
873 KCl, 2 mM MgCl<sub>2</sub>, 1 mM EGTA, 20 mM HEPES, pH 7.2) and incubation for 30 min. Prior to  
874 addition of other proteins, the SLBs were washed 10 times by buffer exchange (always  
875 leaving 20 µl on top of the SLB to avoid damage by drying). We tested the formation of lipid  
876 bilayers and the mobility of lipids in control samples by following the recovery of  
877 fluorescence signal after photobleaching of hexa-histidine tagged GFP (His<sub>6</sub>-GFP) as  
878 described in (Köster et al., 2016).

879

880 *Actin filament polymerization and tethering to SLBs*

881 Actin was purified from muscle acetone powder from rabbit (cat. no. M6890, Merck) and  
882 labelled with Alexa488-maleimide (cat. no. A10254, Thermo Fisher) following standard  
883 protocols (Köster et al., 2016; Pardee & Spudich, 1982).

884 In a typical experiment, actin filaments were polymerized in parallel to SLB formation to  
885 ensure that all components of the experiment were freshly assembled before starting  
886 imaging. First 10%<sub>vol</sub> of 10x ME buffer (100 mM MgCl<sub>2</sub>, 20 mM EGTA, pH 7.2) were mixed  
887 with unlabeled and labeled G-actin (to a final label ratio of 20%), optionally supplemented  
888 with labelled capping protein in G-actin buffer (1 mM CaCl<sub>2</sub>, 0.2mM ATP, 2mM Tris, 0.5 mM  
889 TCEP-HCl, pH 7.2) to a final G-actin concentration of 10 μM and incubated for 2 min to  
890 replace G-actin bound Ca<sup>2+</sup> ions with Mg<sup>2+</sup> ions. Polymerization of actin filaments was  
891 induced by addition of an equal amount of 2x KMEH buffer supplemented with 2 mM Mg-  
892 ATP bringing the G-actin concentration to 5 μM. After 30 min incubation time, actin filaments  
893 were added to the SLBs using blunt-cut pipette tips at a corresponding G-actin concentration  
894 of 100 nM (to ensure a homogenous mix of actin filaments, 2 μl of actin filament solution was  
895 mixed in 18 μl KMEH and then added to the SLB containing 80 μl KMEH). After 10 min of  
896 incubation, His<sub>6</sub>-Curly or other variants of histidine-tagged actin binding proteins at a final  
897 concentration of 10 nM were added and a short time after (1 - 5 min) binding of actin to the  
898 SLB could be observed using TIRF microscopy.  
899

900 In experiments with formin, the SLB was first incubated with 10 nM His<sub>6</sub>-SpCdc12(FH1-FH2)  
901 and 10 nM His<sub>6</sub>-Curly for 20 min, then washed twice with KMEH. During the incubation time,  
902 10%<sub>vol</sub> of 10x ME buffer was mixed with unlabeled and labeled G-actin at 4 μM (final label  
903 ratio of 20%) together with 5 μM profilin and incubated for 5 min prior to addition to the SLB  
904 and imaging with TIRF microscopy.  
905

906 In experiments with tropomyosin or fimbrin, actin filaments ( $C_{G-actin} = 1 \mu M$ ) were incubated  
907 with tropomyosin at a 1:3 protein concentration ratio or with fimbrin at a 3:2 protein  
908 concentration ratio for 15 min prior to addition to the SLB (Palani et al., 2019).  
909

910 In experiments with muscle myosin II filaments, we prepared muscle myosin II filaments by  
911 diluting the stock of muscle myosin II proteins (rabbit, m. psoas, cat. no. 8326-01, Hypermol)  
912 ( $C_{myoII} = 20 \mu M$ ; 500mM KCl, 1mM EDTA, 1 mM DTT, 10 mM HEPES, pH 7.0) 10-times with  
913 MilliQ water to drop the KCl concentration to 50 mM and incubated for 5 min to ensure  
914 myosin filament formation. Myosin II filaments were further diluted in KMEH to 200 nM and  
915 added to the actin filaments bound to the SLB by His<sub>6</sub>-Curly by replacing 1/10 of the sample  
916 buffer with the myosin II filament solution and supplemented with 0.1 mM Mg-ATP as well as  
917 a mix of 1 mM Trolox (cat. no. 648471, Merck), 2 mM protocatechuic acid (cat. no.  
918 03930590, Merck) and 0.1 μM protocatechuate 3,4-dioxygenase (cat. no. P8279, Merck) to  
919 minimize photobleaching. To summarize, the final buffer composition was 50mM KCl, 2mM  
920 MgCl<sub>2</sub>, 1mM EGTA, 20mM HEPES, 0.1mM ATP, 1 mM Trolox, 2 mM protocatechuic acid  
921 and 0.1 μM protocatechuate 3,4-dioxygenase at pH 7.2 containing actin filaments ( $C_{G-actin} =$   
922  $100 \text{ nM}$ ) and myosin II filaments ( $C_{myoII} = 20 \text{ nM}$ ). It was important to keep the pH at 7.2, as  
923 changes in pH would affect motor activity. As reported earlier, myosin filaments started to  
924 show actin network remodeling activity after about 10-15 min of incubation (Köster et al.,  
925 2016; Mosby et al., 2020).  
926

### 927 *TIRF microscopy*

928 Images were acquired using a Nikon Eclipse Ti-E/B microscope equipped with perfect focus  
929 system, a Ti-E TIRF illuminator (CW laser lines: 488nm, 561nm and 640nm) and a Zyla  
930 sCMOS 4.2 camera (Andor, Oxford Instruments, UK) controlled by Andor iQ3 software  
931 (<https://andor.oxinst.com/products/iq-live-cell-imaging-software/>).  
932

### 933 **Image analysis**

934 Images were analyzed using ImageJ (<http://imagej.nih.gov/ij>).  
935 Curvature was measured by fitting ellipses to match the actin filament contour by hand,  
936 while measuring first fully formed rings before curved actin filament segments and by going  
937 from the highest curvatures down to lower curvatures in each image with a cut off for

938 measurements at curvatures smaller than  $0.1 \mu\text{m}^{-1}$  or at 30-40 measurements per image  
939 (see examples in Figure 1 – figure supplement 1D; Figure 1-figure supplement 2B).  
940 To measure the angle of kinks in individual actin filaments, cropped images of individual  
941 actin filaments were processed with a Sobel filter (part of the Mosaic suit for ImageJ,  
942 <http://mosaic.mpi-cbg.de/?q=downloads/imagej>) to highlight the actin filament center, and  
943 the angles were measured manually with the ImageJ angle tool.  
944 The actin ring contraction rate upon myosin II filament action was measured by generating  
945 kymographs based on a line (3 pixels width) dividing the ring into two equal halves.  
946

### 947 **Data plotting and statistics**

948 Graphs were generated using OriginPro (version 2019b, OriginLab, USA). Plots depict  
949 individual data points, mean (circle), median (central line) and standard deviation (top and  
950 bottom lines).  
951

### 952 **Acknowledgement**

953 The authors would like to thank Dr. Gayathri Panangath (IISER Pune, India), Dr. Minhaj  
954 Sirajuddin (Instem, Bangalore, India), for insightful discussions. The work was supported by  
955 a Wellcome Investigator Award (WT 101885MA) and an ERC advanced grant (ERC- 2014-  
956 ADG N° 671083) to MKB. DVK thanks the Wellcome-Warwick Quantitative Biomedicine  
957 Programme for funding (RMRCB0058).  
958

### 959 **Competing Interests**

960 The authors have no competing interests to declare.  
961  
962

### 963 **Video captions**

964  
965 Video 1: TIRF microscopy image sequence of actin filaments (Alexa488) landing on His<sub>6</sub>-  
966 curly decorated SLBs; scale bar: 5  $\mu\text{m}$ .  
967

968 Video 2: Example image sequence of an actin filament (Alexa488) bound to a His<sub>6</sub>-curly  
969 decorated SLB displaying individual bending events after processing the image sequence  
970 with a Sobel filter to highlight the shape of the actin filament (the unprocessed images are  
971 shown in Figure 2-figure supplement 2); scale bar: 1  $\mu\text{m}$ .  
972

973 Video 3: Example image sequence of an actin filament (Alexa488, gray) with the plus end  
974 labelled by capping protein (SNAP647, yellow) landing on a His<sub>6</sub>-curly decorated SLB; scale  
975 bar: 1  $\mu\text{m}$ .  
976

977 Video 4: Example image sequence of an actin filament (Alexa488, gray) with the plus end  
978 labelled by capping protein (SNAP647, cyan) landing on a curly-His<sub>6</sub> decorated SLB; scale  
979 bar: 1  $\mu\text{m}$ .  
980

981 Video 5: Example image sequences of actin filaments (Alexa488) polymerized by SLB  
982 tethered formin in the presence of His<sub>6</sub>-curly bound to the SLB; scale bar 1  $\mu\text{m}$ .  
983

984 Video 6: Example image sequences of actin filaments (Alexa488) decorated with  
985 tropomyosin binding to membrane tethered His<sub>6</sub>-curly; scale bar: 1  $\mu\text{m}$ .  
986

987 Video 7: Example image sequence showing formation, translation, and contraction of actin  
988 filament (Alexa488) rings on membrane tethered His<sub>6</sub>-curly after the addition of muscle  
989 myosin II filaments; scale bar: 1  $\mu\text{m}$ .  
990

991 Video 8: Example image sequences of actin filament (Alexa488) ring contraction on  
992 membrane tethered His<sub>6</sub>-curly after the addition of muscle myosin II filaments; scale bar: 1  
993  $\mu\text{m}$ .  
994  
995

**Table 1: Plasmids used in this study**

996  
997  
998  
999  
1000  
1001

pET28C-6HIS-Rng2(1-189)	pSPW153
pET28C-6HIS-Rng2(1-250)	pSPW155
pET28C-6HIS-Rng2(1-300)	pSPW113
pET28C-6HIS-Rng2(1-147)	pSPW167
pET28C-6HIS-Rng2(41-147)	pSPW169
pET28C-6HIS-Rng2 (41-189)	pSPW187
pET28C-6HIS-Rng2 (41-250)	pSPW189
pET28C-6HIS-Rng2 (41-300)	pSPW191
pETMCN-Rng2(1-189)-C-6HIS	pSPW288
pETMCN-Rng2(1-250)-C-6HIS	pSPW290
pETMCN-Rng2(1-300)-C-6HIS	pSPW291
pET28C-6HIS-Rng2(1-189; $\Delta$ 154-160)	pSPW297
pET28C-6HIS-Rng2(1-300; $\Delta$ 154-160)	pSPW299
pET28C-6HIS-Curly100 (150-250)	pSPW284
pET23a-10HIS-SNAP-Rng2-CHD (1-300)	pSPW195
pET28C-6HIS-Sclqg1 (1-330)	pSPW200
pET28C-6HIS-HslIQGAP1 (1-678)	pSPW293
pCDNA3-EGFP-GSGG-Rng2(1-189)	pSPW620
pET-3d-6HIS-SNAP-tagged $\beta$ 1 subunit and untagged $\alpha$ 1 subunits of chicken CapZ	Addgene: 69948 Bombardier et al., 2015
pET28C-6HIS-Cdc12 (740-1391)	pSPW123
pETMCN-AScdc8	pSPW036
pGEX4T1-GST-Fim1	pSPW114
pET23a-10HIS-SNAP-Ezrin-ABD	pSPW151
pGEX-alpha actinin4 (acnt4)	Gift from L. Blanchoin's lab

1002  
1003  
1004  
1005  
1006  
1007  
1008  
1009  
1010  
1011

## 1012 References

- 1013
- 1014 Almonacid, M., Celton-Morizur, S., Jakubowski, J. L., Dingli, F., Loew, D., Mayeux, A., Chen,  
1015 J. S., Gould, K. L., Clifford, D. M., & Paoletti, A. (2011). Temporal control of contractile  
1016 ring assembly by Plo1 regulation of myosin II recruitment by Mid1/anillin. *Current*  
1017 *Biology*, 21(6), 473–479. <https://doi.org/10.1016/j.cub.2011.02.003>
- 1018 Bieling, P., Li, T.-D., Weichsel, J., McGorty, R., Jreij, P., Huang, B., Fletcher, D. A., &  
1019 Mullins, R. D. (2016). Force Feedback Controls Motor Activity and Mechanical  
1020 Properties of Self-Assembling Branched Actin Networks. *Cell*, 164(1–2), 115–127.  
1021 <https://doi.org/10.1016/j.cell.2015.11.057>
- 1022 Briggs, M. W., & Sacks, D. B. (2003). IQGAP proteins are integral components of  
1023 cytoskeletal regulation. *EMBO Reports*, 4(6), 571–574.  
1024 <https://doi.org/10.1038/sj.embor.embor867>
- 1025 De La Cruz, E. M., & Gardel, M. L. (2015). Actin mechanics and fragmentation. *Journal of*  
1026 *Biological Chemistry*, 290(28), 17137–17144. <https://doi.org/10.1074/jbc.R115.636472>
- 1027 Eng, K., Naqvi, N. I., Wong, K. C. Y., & Balasubramanian, M. K. (1998). Rng2p, a protein  
1028 required for cytokinesis in fission yeast, is a component of the actomyosin ring and the  
1029 spindle pole body. *Current Biology*, 8(11), 611–621. [https://doi.org/10.1016/S0960-9822\(98\)70248-9](https://doi.org/10.1016/S0960-9822(98)70248-9)
- 1030
- 1031 Epp, J. A., & Chant, J. (1997). An IQGAP-related protein controls actin-ring formation and  
1032 cytokinesis in yeast. *Current Biology*, 7(12), 921–929. [https://doi.org/10.1016/S0960-9822\(06\)00411-8](https://doi.org/10.1016/S0960-9822(06)00411-8)
- 1033
- 1034 Hayakawa, Y., Takaine, M., Imai, T., Yamada, M., Hirose, K., Tokuraku, K., Ngo, K. X.,  
1035 Kodera, N., Numata, O., Nakano, K., & Uyeda, T. Q. P. (2020). Actin binding domain of  
1036 Rng2 strongly inhibits actin movement on myosin II HMM through structural changes of  
1037 actin filaments. *BioRxiv*.
- 1038 Köster, D. V., Husain, K., Iljazi, E., Bhat, A., Bieling, P., Mullins, R. D., Rao, M., & Mayor, S.  
1039 (2016). Actomyosin dynamics drive local membrane component organization in an in  
1040 vitro active composite layer. *Proceedings of the National Academy of Sciences*,  
1041 113(12), E1645–E1654. <https://doi.org/10.1073/pnas.1514030113>
- 1042 Kruppa, A. J., Kishi-Itakura, C., Masters, T. A., Rorbach, J. E., Grice, G. L., Kendrick-Jones,  
1043 J., Nathan, J. A., Minczuk, M., & Buss, F. (2018). Myosin VI-Dependent Actin Cages  
1044 Encapsulate Parkin-Positive Damaged Mitochondria. *Developmental Cell*, 44(4), 484-  
1045 499.e6. <https://doi.org/10.1016/j.devcel.2018.01.007>
- 1046 Kučera, O., Janda, D., Siahaan, V., Dijkstra, S. H., Pilátová, E., Zatecka, E., Diez, S., Braun,  
1047 M., & Lansky, Z. (2020). Anillin propels myosin-independent constriction of actin rings.  
1048 *BioRxiv*, 1–27. <https://doi.org/10.1101/2020.01.22.915256>
- 1049 Kumari, A., Kesarwani, S., Javoor, M. G., Vinothkumar, K. R., & Sirajuddin, M. (2020).  
1050 Structural insights into actin filament recognition by commonly used cellular actin  
1051 markers. *The EMBO Journal*, 846337. <https://doi.org/10.15252/embj.2019104006>
- 1052 Laplante, C., Huang, F., Tebbs, I. R., Bewersdorf, J., & Pollard, T. D. (2016). Molecular  
1053 organization of cytokinesis nodes and contractile rings by super-resolution fluorescence  
1054 microscopy of live fission yeast. *Proceedings of the National Academy of Sciences*,  
1055 113(40), E5876–E5885. <https://doi.org/10.1073/pnas.1608252113>
- 1056 Laporte, D., Coffman, V. C., Lee, I. J., & Wu, J. Q. (2011). Assembly and architecture of  
1057 precursor nodes during fission yeast cytokinesis. *Journal of Cell Biology*, 192(6), 1005–  
1058 1021. <https://doi.org/10.1083/jcb.201008171>
- 1059 Li, Y., & Munro, E. (2020). Existing actin filaments orient new filament growth to provide  
1060 structural memory of filament alignment during cytokinesis. *BioRxiv*.  
1061 <https://doi.org/10.1101/2020.04.13.039586>
- 1062 Litschel, T., Kelley, C. F., Holz, D., Koudehi, M. A., Vogel, S. K., Burbaum, L., Mizuno, N.,  
1063 Vavylonis, D., & Schwille, P. (2020). Reconstitution of contractile actomyosin rings in  
1064 vesicles. *BioRxiv*. <https://doi.org/10.1101/2020.06.30.180901>
- 1065 Mavrakis, M., Azou-Gros, Y., Tsai, F.-C., Alvarado, J., Bertin, A., Iv, F., Kress, A., Basselet,  
1066 S., Koenderink, G. H., & Lecuit, T. (2014). Septins promote F-actin ring formation by  
1067 crosslinking actin filaments into curved bundles. *Nature Cell Biology*, 16(4), 322–334.  
1068 <https://doi.org/10.1038/ncb2921>
- 1069 Mishra, M., Kashiwazaki, J., Takagi, T., Srinivasan, R., Huang, Y., Balasubramanian, M. K.,

- 1070 & Mabuchi, I. (2013). In vitro contraction of cytokinetic ring depends on myosin II but  
1071 not on actin dynamics. *Nature Cell Biology*, 15(7), 853–859.  
1072 <https://doi.org/10.1038/ncb2781>
- 1073 Mosby, L. S., Hundt, N., Young, G., Fineberg, A., Polin, M., Mayor, S., Kukura, P., & Köster,  
1074 D. V. (2020). Myosin II Filament Dynamics in Actin Networks Revealed with  
1075 Interferometric Scattering Microscopy. *Biophysical Journal*, 118(8), 1946–1957.  
1076 <https://doi.org/10.1016/j.bpj.2020.02.025>
- 1077 Murrell, M. P., & Gardel, M. L. (2012). F-actin buckling coordinates contractility and severing  
1078 in a biomimetic actomyosin cortex. *Proceedings of the National Academy of Sciences  
1079 of the United States of America*, 19. <https://doi.org/10.1073/pnas.1214753109>
- 1080 Narita, A. (2020). ADF/cofilin regulation from a structural viewpoint. *Journal of Muscle  
1081 Research and Cell Motility*, 41(1), 141–151. <https://doi.org/10.1007/s10974-019-09546-6>
- 1082 6
- 1083 Nye, J. A., & Groves, J. T. (2008). Kinetic control of histidine-tagged protein surface density  
1084 on supported lipid bilayers. *Langmuir: The ACS Journal of Surfaces and Colloids*,  
1085 24(8), 4145–4149. <https://doi.org/10.1021/la703788h>
- 1086 Padmanabhan, A., Bakka, K., Sevugan, M., Naqvi, N. I., D'Souza, V., Tang, X., Mishra, M.,  
1087 & Balasubramanian, M. K. (2011). IQGAP-related Rng2p organizes cortical nodes and  
1088 ensures position of cell division in fission yeast. *Current Biology*, 21(6), 467–472.  
1089 <https://doi.org/10.1016/j.cub.2011.01.059>
- 1090 Palani, S., Köster, D. V., Hatano, T., Kamnev, A., Kanamaru, T., Brooker, H. R., Hernandez-  
1091 Fernaund, J. R., Jones, A. M. E., Millar, J. B. A., Mulvihill, D. P., & Balasubramanian, M.  
1092 K. (2019). Phosphoregulation of tropomyosin is crucial for actin cable turnover and  
1093 division site placement. *The Journal of Cell Biology*, jcb.201809089.  
1094 <https://doi.org/10.1083/jcb.201809089>
- 1095 Pardee, J. D., & Spudich, J. A. (1982). Purification of muscle actin. *Methods in Cell Biology*,  
1096 24, 271–289. <http://www.ncbi.nlm.nih.gov/pubmed/7098993>
- 1097 Skau, C. T., & Kovar, D. R. (2010). Fimbrin and tropomyosin competition regulates  
1098 endocytosis and cytokinesis kinetics in fission yeast. *Current Biology*, 20(16), 1415–  
1099 1422. <https://doi.org/10.1016/j.cub.2010.06.020>
- 1100 Skoumpla, K., Coulton, A. T., Lehman, W., Geeves, M. A., & Mulvihill, D. P. (2007).  
1101 Acetylation regulates tropomyosin function in the fission yeast *Schizosaccharomyces  
1102 pombe*. *Journal of Cell Science*, 120(9), 1635–1645. <https://doi.org/10.1242/jcs.001115>
- 1103 Swulius, M. T., Nguyen, L. T., Ladinsky, M. S., Ortega, D. R., Aich, S., Mishra, M., & Jensen,  
1104 G. J. (2018). Structure of the fission yeast actomyosin ring during constriction.  
1105 *Proceedings of the National Academy of Sciences of the United States of America*,  
1106 115(7), E1455–E1464. <https://doi.org/10.1073/pnas.1711218115>
- 1107 Taylor, K. A., Taylor, D. W., & Schachat, F. (2000). Isoforms of  $\alpha$ -actinin from cardiac,  
1108 smooth, and skeletal muscle form polar arrays of actin filaments. *Journal of Cell  
1109 Biology*, 149(3), 635–645. <https://doi.org/10.1083/jcb.149.3.635>
- 1110 Tebbs, I. R., Pollard, T. D., & D, P. T. (2013). Separate roles of IQGAP Rng2p in forming  
1111 and constricting the *Schizosaccharomyces pombe* cytokinetic contractile ring.  
1112 *Molecular Biology of the Cell*, 24(12), 1904–1917. <https://doi.org/10.1091/mbc.E12-10-0775>
- 1113 0775
- 1114 Toyoshima, Y. Y., Kron, S. J., & Spudicht, J. A. (1990). The myosin step size: Measurement  
1115 of the unit displacement per ATP hydrolyzed in an in vitro assay  
1116 (actin/crossbridge/muscle contraction). In *Proc. Nati. Acad. Sci. USA* (Vol. 87, Issue  
1117 September).
- 1118 Vassilopoulos, S., Gibaud, S., Jimenez, A., Caillol, G., & Leterrier, C. (2019). Ultrastructure  
1119 of the axonal periodic scaffold reveals a braid-like organization of actin rings. *Nature  
1120 Communications*, 10(1), 636217. <https://doi.org/10.1038/s41467-019-13835-6>
- 1121 Wang, C.-H., Balasubramanian, M. K., & Dokland, T. (2004). Structure, crystal packing and  
1122 molecular dynamics of the calponin-homology domain of *Schizosaccharomyces pombe*  
1123 Rng2. *Acta Crystallographica Section D Biological Crystallography*, 60(8), 1396–1403.  
1124 <https://doi.org/10.1107/S0907444904012983>
- 1125 Way, M., Sanders, M., Garcia, C., Sakai, J., & Matsudaira, P. (1995). Sequence and domain  
1126 organization of scruin, an actin-cross-linking protein in the acrosomal process of  
1127 *Limulus* sperm. *Journal of Cell Biology*, 128(1–2), 51–60.

1128 Xu, K., Zhong, G., & Zhuang, X. (2013). Actin, spectrin, and associated proteins form a  
1129 periodic cytoskeletal structure in axons. *Science (New York, N.Y.)*, 339(6118), 452–  
1130 456. <https://doi.org/10.1126/science.1232251>  
1131